Analytic Theory of Edge Localized Mode Suppression by Static Resonant Magnetic Perturbations in H-mode Tokamak Discharges

Richard Fitzpatrick

Institute for Fusion Studies, Department of Physics, University of Texas at Austin, Austin TX, 78712, USA

E-mail: rfitzp@farside.ph.utexas.edu

Abstract. An analytic theory of edge localized mode (ELM) suppression in an H-mode tokamak plasma via the application of a static, externally generated, resonant magnetic perturbation (RMP) is presented. This theory is based on the plausible hypothesis that mode penetration at the top of the pedestal is a necessary and sufficient condition for the RMP-induced suppression of ELMs. The theory also makes use of a number of key insights gained in a recent publication (Fitzpatrick R 2019). The first insight is that the response of the plasma to a particular helical component of the RMP, in the immediate vicinity of the associated resonant surface, is governed by nonlinear magnetic island physics, rather than by linear layer physics. The second insight is that neoclassical effects play a vital role in the physics of RMP-induced ELM suppression. The final insight is that plasma impurities play an important role in the physics of RMP-induced ELM suppression. The theory presented in this paper is employed to gain a better understanding of ELM suppression in DIII-D and ITER H-mode discharges. It is found that ELM suppression is only possible when q_{95} takes values that lie in certain narrow windows. Moreover, the widths of these windows decrease with increasing plasma density. Assuming a core plasma rotation of 20 krad/s, the window width for a model ITER H-mode discharge is found to be similar to, but slightly smaller than, the window width in a typical DIII-D H-mode discharge.

1. Introduction

1.1. Motivation for RMP-Generated ELM Suppression

Tokamak discharges operating in high-confinement mode (H-mode) [1] exhibit intermittent bursts of heat and particle transport, emanating from the outer regions of the plasma, that are known as *type-I edge localized modes* (ELMs) [2]. ELMs are fairly harmless in present-day tokamaks possessing carbon plasma-facing components. However, large ELMs can cause a problematic influx of tungsten ions into the plasma core in tokamaks possessing tungsten plasma-facing components [3]. Moreover, it is estimated that the heat load that ELMs will deliver to the tungsten plasma-facing components in a reactor-scale tokamak, such as ITER, will be large enough to cause massive tungsten ion influx into the core, and that the erosion associated with this process will unacceptably limit the lifetimes of these components [4]. Consequently, the development of robust and effective methods for ELM control is a high priority for the international magnetic fusion program.

The most promising method for the control of ELMs in H-mode tokamak discharges is via the application of static *resonant magnetic perturbations* (RMPs). Complete RMP-induced ELM suppression was first demonstrated on the DIII-D tokamak [5]. Subsequently, either mitigation or compete suppression of ELMs has been demonstrated on the JET [6], ASDEX-U [7], KSTAR [8], and EAST [9] tokamaks.

1.2. Observed Features of RMP-Generated ELM Suppression

ELMs are thought to be caused by peeling-ballooning instabilities, with intermediate toroidal mode numbers, that are driven by the strong pressure and current density gradients characteristic of the edge region of an H-mode tokamak discharge [10], which is generally known as the *pedestal* region. The initial observations of RMP-induced ELM suppression were interpreted as an indication that the magnetic field in the pedestal is rendered stochastic by an applied RMP, leading to greatly enhanced transport via thermal diffusion along magnetic field-lines [5, 11]. This explanation was quickly abandoned because no significant reduction in the electron temperature gradient in the pedestal is observed during RMP-induced ELM suppression experiments, whereas a very significant reduction would be expected in the presence of stochastic fields. It is now generally accepted that response currents generated within the pedestal, as a consequence of plasma rotation, play a crucial role in the perturbed equilibrium in the presence of RMPs, and that these currents act to prevent the formation of RMP-driven magnetic island chains—a process known as *shielding*—and, thereby, significantly reduce the stochasticity of the magnetic field [12].

The application of a static RMP, resonant in the pedestal region, to an H-mode tokamak discharge is observed to give rise to two distinct phenomena [13, 14, 15, 16, 17]. The first of these is the so-called *density pump-out*, which is characterized by a reduction in the electron number density in the pedestal region that varies smoothly with the amplitude of the applied RMP, is accompanied by a similar, but significantly smaller, reduction in the electron and ion temperatures, but is not associated with ELM suppression. The second phenomenon is *mode penetration*, which occurs when the amplitude of the applied RMP exceeds a certain threshold value, is accompanied by sudden changes in the electron number density, electron and ion temperature, and ion toroidal angular velocity, profiles in the pedestal region, and,

most importantly, is associated with the suppression of ELMs. Mode penetration is only observed to take place when q_{95} (i.e., the safety-factor on the magnetic flux-surface that encloses 95% of the poloidal flux enclosed by the last closed flux-surface) takes values that lie in certain narrow windows [15, 16]. Furthermore, the mode penetration threshold is observed to increase markedly with increasing electron number density [15, 16].

1.3. Recent Advances in Theory of RMP-Generated ELM Suppression

Recent research [18] has shed considerable light on the hitherto poorly understood physical mechanism that underlies RMP-induced ELM suppression in H-mode tokamak discharges. In particular, computer simulations (made using the cylindrical, multi-harmonic, five-field, nonlinear, initial-value code, TM1 [19, 20, 21]) of RMP-induced ELM suppression experiments performed on the DIII-D tokamak conclude that the density pump-out phenomenon is associated with the formation of a locked magnetic island chain at the bottom of the pedestal, whereas the mode penetration phenomenon is associated with the formation of a locked magnetic island chain at the top of the pedestal.

As described below, the markedly different responses of the plasma to helical components of the applied RMP that are resonant at the bottom and at the top of the pedestal—which is the main finding of the simulations described in [18]—can be accounted for on the basis of standard mode locking theory [22, 23].

The plasma at the bottom of the pedestal is too cold and resistive for plasma rotation to effectively shield any locally resonant components of the applied RMP [24]. Hence, if one of the helical harmonics of the RMP is resonant close to the bottom of the pedestal then it generates a locked magnetic island chain whose width is similar to the associated vacuum island chain (i.e., the island chain produced by naively superimposing the vacuum RMP onto the equilibrium plasma magnetic field). This island chain causes a local flattening of the density and temperature profiles [25]. However, because the equilibrium density gradient at the bottom of the pedestal invariably greatly exceeds the temperature gradient (i.e., because $n_e/(T_e\,\eta_i)\,[10^{\,19}\,\mathrm{m}^{\,-3}/(\mathrm{keV})] \gg 1$; see Figures 2 and 7 and [24]), this flattening produces a much more marked reduction in the pedestal density (measured in units of $10^{\,19}\,\mathrm{m}^{-3}$) than in the pedestal temperature (measured in units of keV). In other words, the flattening is responsible for the density pump-out phenomenon [18].

On the other hand, the plasma at the top of the pedestal is sufficiently hot that plasma rotation is capable of strongly shielding any locally resonant components of the applied RMP. Hence, if one of the helical harmonics of the RMP is resonant close to the top of the pedestal then it generates an island chain whose width is much smaller than the associated vacuum island chain, and, consequently, has little effect on the local density and temperature profiles. However, if the amplitude of the resonant harmonic exceeds a certain critical value then torque balance at the resonant surface breaks down, resulting in the sudden arrest of the local plasma rotation, and the complete breakdown of shielding [22, 23]. This so-called mode penetration phenomenon is associated with the generation of a locked magnetic island chain at the resonant surface whose width is similar to the vacuum island width. Such an island chain produces a local flattening of the plasma density and temperature profiles that is presumably sufficiently strong to prevent the plasma in the pedestal region from ever exceeding the peeling-ballooning stability threshold. In fact, the fundamental

hypothesis of both [18] and this paper is that mode penetration at the top of the pedestal is directly responsible for ELM suppression. This hypothesis allows us to model ELM suppression by modelling mode penetration, which is a comparatively straightforward task, rather than by directly modelling ELMs, which is a very much more complicated task.

1.4. Further Advances in Theory of RMP-Generated ELM Suppression

Recent research [24], motivated by [18], has lead to three key insights regarding the physics of mode penetration in the pedestal region of an H-mode tokamak discharge.

The first insight is that, in the immediate vicinity of the associated resonant surface, the response of the pedestal plasma to a particular helical component of the applied RMP is governed by *nonlinear* magnetic island physics, rather than by *linear* layer physics. The key point is that, although plasma rotation at the top of the pedestal is capable of strongly shielding any locally resonant component of the RMP, this shielding is not strong enough to reduce the width of the driven magnetic island chain below the linear layer width (which is very small in a high temperature tokamak plasma). The fact that the shielded state is governed by nonlinear island physics, rather than by linear layer physics, has two important consequences. First, the shielded state consists of a narrow, *rotating*, magnetic island chain whose width *pulsates*, rather than the constant-width locked island chain (whose width must, of course, be less than the linear layer width) predicted by linear physics [23, 26, 27, 28]. (Incidentally, pulsating islands have been observed experimentally—see Figure 29 of [29].) Second, the so-called *natural phase velocity* of the driven island chain (which is defined as the helical phase velocity of the corresponding naturally unstable island chain in the absence of the RMP [22]) predicted by nonlinear island theory is quite different to that predicted by linear layer theory. This is significant because both the degree of shielding at the resonant surface and the mode penetration threshold depend crucially on the natural phase velocity [22]. According to linear layer theory, a naturally unstable magnetic island chain propagates in the *electron* diamagnetic direction relative to the $\mathbf{E}\times\mathbf{B}$ frame at the resonant surface [30]. On the other hand, according to nonlinear island theory, a naturally unstable magnetic island chain propagates in the *ion* diamagnetic direction relative to the local $\mathbf{E}\times\mathbf{B}$ frame [27, 28]. Incidentally, there is clear experimental confirmation that a naturally unstable nonlinear magnetic island chain in a tokamak plasma propagates in the ion, rather than the electron, diamagnetic direction relative to the local $\mathbf{E}\times\mathbf{B}$ frame [31, 32].

The second insight is that *neoclassical* effects play a crucial role in the physics of mode penetration in the pedestal region of an H-mode tokamak discharge. This is the case, firstly, because intrinsic neoclassical poloidal rotation is the main controlling factor that determines the natural phase velocity of a nonlinear magnetic island chain (relative to the local $\mathbf{E}\times\mathbf{B}$ frame) [27, 28], secondly, because neoclassical poloidal flow-damping plays a very significant role in determining the mode penetration threshold [24], and, finally, because the neoclassical modification of the plasma electrical conductivity is particularly large in the outer regions of a typical H-mode tokamak discharge (because of the large fraction of trapped particles), and must, therefore, be taken into account in order to accurately calculate the plasma response to an applied RMP at a resonant surface lying in the pedestal region.

The final insight is that plasma *impurities* play an important role in the physics of mode penetration in the pedestal region of an H-mode tokamak discharge. This is

the case because the presence of experimentally observed levels of plasma impurities can significantly modify the intrinsic neoclassical poloidal rotation, the neoclassical poloidal flow-damping rate, and the classical plasma electrical conductivity, in the outer regions of an H-mode discharge [24].

1.5. Purpose of Paper

The purpose of this paper is to improve the model of RMP-induced mode penetration in the pedestal region of an H-mode tokamak plasma that was derived in [24], and then to use the model to gain a better understanding of the physics of ELM suppression by RMPs. The former goal is achieved, firstly, by fully incorporating the well-known moment-based neoclassical theory of Hirshman and Sigmar into the model [33], secondly, by allowing for non-trace amounts of plasma impurities, and, finally, by incorporating some useful mode penetration results that were first derived in [26].

2. Preliminary Analysis

2.1. Plasma Equilibrium

Consider an axisymmetric tokamak plasma equilibrium whose magnetic and electric fields take the forms [33]

$$\mathbf{B} = I\,\nabla\phi + \nabla\phi\times\nabla\psi, \tag{1}$$

$$\mathbf{E} = -\nabla\Phi + E_\parallel\,\mathbf{b}, \tag{2}$$

respectively, where $\mathbf{b} = \mathbf{B}/B$, $I = I(\psi)$, and $\Phi = \Phi(\psi)$. Here, ϕ is the geometric toroidal angle, which implies that $|\nabla\phi| = 1/R$, where R is the perpendicular distance from the toroidal symmetry axis. Furthermore, ψ is the poloidal magnetic flux (which is a convenient label for magnetic flux surfaces), whereas Φ is the electric scalar potential.

It is helpful to define a "straight" poloidal angle, θ, which increases by 2π radians for every poloidal circuit around a magnetic flux surface, and which is such that

$$\nabla\psi\cdot\nabla\theta\times\nabla\phi \equiv \mathbf{B}\cdot\nabla\theta = \frac{I}{R^2\,q}, \tag{3}$$

where $q(\psi)$ is the so-called safety factor. It follows that

$$\mathbf{B}\cdot\nabla = \frac{I}{R^2}\left(\frac{\partial}{\partial\phi} + \frac{1}{q}\,\frac{\partial}{\partial\theta}\right). \tag{4}$$

It is also helpful to define a "geometric" poloidal angle [33],

$$\Theta = 2\pi\int_0^\theta \frac{d\theta'}{\mathbf{b}\cdot\nabla\theta'}\Bigg/\oint\frac{d\theta'}{\mathbf{b}\cdot\nabla\theta'}. \tag{5}$$

It is easily demonstrated that

$$\mathbf{b}\cdot\nabla\Theta = \mathbf{b}\cdot\nabla\Theta(\psi). \tag{6}$$

2.2. Useful Definitions

The plasma is assumed to be made up of a number of distinct species. Let m_a, e_a, $n_a(\psi)$, $T_a(\psi)$, and $p_a = n_a\,T_a$ be the mass, electric charge, number density, temperature (in energy units), and pressure, respectively, of species a. The species-a thermal velocity takes the form

$$v_{T\,a} = \sqrt{\frac{2\,T_a}{m_a}}. \tag{7}$$

It is helpful to define the species-a collision time, τ_{aa}, where [33]

$$\frac{1}{\tau_{aa}} = \frac{4}{3\sqrt{\pi}}\,\frac{4\pi\,n_a\,e_a^{\,4}\,\ln\Lambda}{(4\pi\,\epsilon_0)^{\,2}\,m_a^2\,v_{T\,a}^3}, \tag{8}$$

and the Coulomb logarithm, $\ln\Lambda$, is assumed to take the same large constant value (i.e., $\ln\Lambda \simeq 17$), independent of species.

The flux-surface average operator, $\langle\cdots\rangle$, is defined [33]

$$\langle A\rangle(\psi) = \oint \frac{A(\psi,\theta)\,d\theta}{\mathbf{B}\cdot\nabla\theta}\Bigg/\oint\frac{d\theta}{\mathbf{B}\cdot\nabla\theta} = \oint\frac{A(\psi,\Theta)\,d\Theta}{B(\psi,\Theta)}\Bigg/\oint\frac{d\Theta}{B(\psi,\Theta)}, \tag{9}$$

where use has been made of (6). Finally, the transit frequency of species a takes the form

$$\omega_{t\,a} = \frac{v_{T\,a}}{L_c}, \tag{10}$$

where [33]

$$L_c = \frac{\langle B^{\,2}\rangle^{\,2}}{\langle(\mathbf{b}\cdot\nabla B)^{\,2}\,\rangle\,|\langle\mathbf{B}\cdot\nabla\theta\rangle|} \times\sum_{k>0}\frac{2}{k}\left[\langle\sin(k\,\Theta)\,(\mathbf{b}\cdot\nabla\ln B)\rangle\,\left\langle\sin(k\,\Theta)\,\frac{(\mathbf{b}\cdot\nabla\ln B)}{B}\right\rangle\right] \tag{11}$$

is the flux-surface-averaged magnetic connection length.

In the banana collisionality regime, the fraction of circulating particles on a given magnetic flux-surface is written [33]

$$f_c = \frac{3}{4}\,\langle B^{\,2}\rangle\int_0^{1/B_{\max}}\frac{\lambda\,d\lambda}{\langle\sqrt{1-\lambda\,B}\rangle}. \tag{12}$$

Finally, the dimensionless species-a collisionality parameter takes the form [33]

$$\nu_{*\,a} = \frac{8}{3\pi}\,\frac{\langle B^{\,2}\rangle}{\langle(\mathbf{b}\cdot\nabla B)^{\,2}\rangle}\,\frac{g\,\omega_{t\,a}}{v_{T\,a}^2\,\tau_{aa}}, \tag{13}$$

where

$$g = \frac{1-f_c}{f_c}. \tag{14}$$

2.3. Model Magnetic Equilibrium

In the paper, for the sake of simplicity, we shall adopt a model magnetic equilibrium characterized by

$$R(r,\Theta) = R_0\,(1+\epsilon\,\cos\Theta), \tag{15}$$

$$B(r,\Theta) = \frac{B_0}{1+\epsilon\,\cos\Theta}. \tag{16}$$

Here, R_0 and B_0 are the major radius and toroidal magnetic field-strength, respectively, on the magnetic axis. Furthermore, $\epsilon = r/R_0$ where r is a flux-surface label with the dimensions of length. The magnetic axis lies at $r = 0$, whereas the plasma boundary is assumed to lie at $r = a$. Of course, $I = B_0\,R_0$ and $a/R_0 < 1$. Strictly speaking, our model is only appropriate to a large aspect-ratio, low-β, tokamak equilibrium whose magnetic flux-surfaces possess circular poloidal cross-sections.

It is easily demonstrated that

$$|\nabla\Theta| = \frac{1}{r}, \tag{17}$$

$$\tan\left(\frac{\theta}{2}\right) = \left(\frac{1-\epsilon}{1+\epsilon}\right)^{1/2}\tan\left(\frac{\Theta}{2}\right), \tag{18}$$

$$\langle B^{\,2}\rangle = \frac{B_0^2}{(1-\epsilon^{\,2})^{\,1/2}}, \tag{19}$$

$$\langle(\mathbf{b}\cdot\nabla B)^{\,2}\rangle = \frac{B_0^2\,\epsilon^{\,2}}{2\,R_0^2\,q^{\,2}\,(1-\epsilon^{\,2})^{\,5/2}}, \tag{20}$$

$$\langle\mathbf{B}\cdot\nabla\theta\rangle = \langle\mathbf{B}\cdot\nabla\Theta\rangle = \frac{B_0}{R_0\,q\,(1-\epsilon^{\,2})^{\,1/2}}, \tag{21}$$

$$\langle\sin(k\,\Theta)\,(\mathbf{b}\cdot\nabla\ln B)\rangle = -\frac{\epsilon\,\delta_{k1}}{2\,R_0\,q\,(1-\epsilon^{\,2})^{\,1/2}}, \tag{22}$$

$$\left\langle \sin\Theta\,\frac{(\mathbf{b}\cdot\nabla\ln B)}{B}\right\rangle = -\frac{\epsilon}{2\,R_0\,q\,B_0\,(1-\epsilon^{\,2})^{\,1/2}}. \tag{23}$$

Hence, (10), (11), and (13) yield

$$\omega_{t\,a} = \frac{v_{T\,a}}{R_0\,|q|\,(1-\epsilon^{\,2})}, \tag{24}$$

$$\nu_{*\,a} = \frac{16}{3\pi}\frac{g}{\epsilon^{\,2}\,\omega_{t\,a}\,\tau_{aa}}. \tag{25}$$

Finally, it is well-known that [34]

$$f_c \simeq 1 - 1.46\,\epsilon^{\,1/2} + 0.46\,\epsilon^{\,3/2}. \tag{26}$$

3. Neoclassical Theory

3.1. Plasma Species

In the following, we shall assume that the plasma consists of three species; namely, electrons (e), majority ions (i), and impurity ions (I). The charges of the three species are $e_e = -e$, $e_i = e$, and $e_I = Z_I\,e$, respectively, where e is the magnitude of the electron charge. Incidentally, in all of the calculations presented in this paper,

the mean impurity ion charge number, Z_I, for a given impurity species is determined as a function of the electron temperature and density using data obtained from the FLYCHK code [35]. Of course, quasi-neutrality demands that

$$n_e = n_i + Z_I\, n_I. \tag{27}$$

It is helpful to define the effective ion charge number,

$$Z_{\rm eff} = \frac{n_i + Z_I^2\, n_I}{n_e}. \tag{28}$$

It follows from the previous two equations that

$$\frac{n_i}{n_e} = \frac{Z_I - Z_{\rm eff}}{Z_I - 1}, \tag{29}$$

$$\frac{n_I}{n_e} = \frac{Z_{\rm eff} - 1}{Z_I\,(Z_I - 1)}. \tag{30}$$

It is also helpful to define

$$\alpha \equiv \frac{n_I\, Z_I^2}{n_i} = \frac{Z_I\,(Z_{\rm eff} - 1)}{Z_I - Z_{\rm eff}}, \tag{31}$$

$$Z_{{\rm eff}\,i} \equiv \frac{n_i}{n_e} = \frac{Z_I - Z_{\rm eff}}{Z_I - 1}, \tag{32}$$

$$Z_{{\rm eff}\,I} \equiv \frac{n_I\, Z_I^2}{n_e} = \frac{Z_I\,(Z_{\rm eff} - 1)}{Z_I - 1}. \tag{33}$$

Note that $Z_{\rm eff} = Z_{{\rm eff}\,i} + Z_{{\rm eff}\,I}$.

3.2. Ion Collisional Friction Matrices

Let

$$x_{ab} = \frac{v_{T\,b}}{v_{T\,a}}. \tag{34}$$

In the following, all quantities that are of order $(m_e/m_i)^{\,1/2}$, $(m_e/m_I)^{\,1/2}$, or smaller, are neglected with respect to unity. The 2×2 dimensionless ion collisional friction matrices, $F^{\,ii}$, $F^{\,iI}$, $F^{\,Ii}$, and $F^{\,II}$, are defined to have the following elements [33, 34]:

$$F^{ii}_{00} = \frac{\alpha\,(1 + m_i/m_I)}{(1 + x_{iI})^{\,3/2}}, \tag{35}$$

$$F^{ii}_{01} = \frac{3}{2}\,\frac{\alpha\,(1 + m_i/m_I)}{(1 + x_{iI}^2)^{\,5/2}}, \tag{36}$$

$$F^{ii}_{10} = F^{ii}_{01}, \tag{37}$$

$$F^{ii}_{11} = \sqrt{2} + \frac{\alpha\,[13/4 + 4\,x_{iI}^2 + (15/2)\,x_{iI}^4]}{(1 + x_{iI}^2)^{\,5/2}}, \tag{38}$$

$$F^{iI}_{00} = F^{ii}_{00}, \tag{39}$$

$$F^{iI}_{01} = \frac{3}{2}\,\frac{T_i}{T_I}\,\frac{\alpha\,(1 + m_I/m_i)}{x_{iI}\,(1 + x_{Ii}^2)^{\,5/2}}, \tag{40}$$

$$F^{iI}_{10} = F^{ii}_{01}, \tag{41}$$

$$F^{iI}_{11} = \frac{27}{4}\,\frac{T_i}{T_I}\,\frac{\alpha\, x_{iI}^2}{(1 + x_{iI}^2)^{\,5/2}}, \tag{42}$$

$$F_{00}^{Ii} = F_{00}^{ii}, \tag{43}$$

$$F_{01}^{Ii} = F_{01}^{ii}, \tag{44}$$

$$F_{10}^{Ii} = F_{01}^{iI}, \tag{45}$$

$$F_{11}^{Ii} = \frac{27}{4}\,\frac{\alpha\, x_{iI}^2}{(1+x_{iI}^2)^{\,5/2}}, \tag{46}$$

$$F_{00}^{II} = F_{00}^{ii}, \tag{47}$$

$$F_{01}^{II} = F_{01}^{iI}, \tag{48}$$

$$F_{10}^{II} = F_{01}^{iI}, \tag{49}$$

$$F_{11}^{II} = \frac{T_i}{T_I}\left\{\sqrt{2}\,\alpha^{\,2}\,x_{Ii} + \frac{\alpha\,[15/2 + 4\,x_{iI}^2 + (13/4)\,x_{iI}^4]}{(1+x_{iI}^2)^{\,5/2}}\right\}. \tag{50}$$

Note that $F_{0j}^{ii} = F_{0j}^{Ii}$, $F_{0j}^{iI} = F_{0j}^{II}$, $F_{j0}^{ii} = F_{j0}^{iI}$, and $F_{j0}^{Ii} = F_{j0}^{II}$, where $j = 0,\, 1$.

3.3. Electron Collisional Friction Matrices

The 2×2 dimensionless electron collisional friction matrices, $F^{\,ee}$, $F^{\,ei}$, and $F^{\,eI}$, are defined to have the following elements [33]:

$$F_{00}^{ee} = Z_{\rm eff}, \tag{51}$$

$$F_{01}^{ee} = \frac{3}{2}\,Z_{\rm eff}, \tag{52}$$

$$F_{10}^{ee} = \frac{3}{2}\,Z_{\rm eff}, \tag{53}$$

$$F_{11}^{ee} = \sqrt{2} + \frac{13}{4}\,Z_{\rm eff}, \tag{54}$$

$$F_{00}^{ei} = Z_{{\rm eff}\,i}, \tag{55}$$

$$F_{01}^{ei} = 0, \tag{56}$$

$$F_{10}^{ei} = \frac{3}{2}\,Z_{{\rm eff}\,i}, \tag{57}$$

$$F_{11}^{ei} = 0, \tag{58}$$

$$F_{00}^{eI} = Z_{{\rm eff}\,I}, \tag{59}$$

$$F_{01}^{eI} = 0, \tag{60}$$

$$F_{10}^{eI} = \frac{3}{2}\,Z_{{\rm eff}\,I}, \tag{61}$$

$$F_{11}^{eI} = 0. \tag{62}$$

Note that $F_{j0}^{ee} = F_{j0}^{ei} + F_{j0}^{eI}$, where $j = 0,\, 1$.

3.4. Neoclassical Viscosity Matrices

The 2×2 dimensionless species-a neoclassical viscosity matrix, $\mu^{\,a}$, is defined to have the following elements [33]:

$$\mu_{00}^{a} = K_{00}^{a}, \tag{63}$$

$$\mu_{01}^a = \frac{5}{2}\,K_{00}^a - K_{01}^a, \tag{64}$$

$$\mu_{10}^a = \mu_{01}^a, \tag{65}$$

$$\mu_{11}^a = K_{11}^a - 5\,K_{01}^a + \frac{25}{4}\,K_{00}^a. \tag{66}$$

Here,

$$K_{ab}^e = g\,\frac{4}{3\sqrt{\pi}}\int_0^\infty \frac{e^{-x}\,x^{\,4+a+b}\,\nu_D^e(x)\,dx}{[x^{\,2}+\nu_{*\,e}\,\nu_D^e(x)]\,[x^{\,2}+(5\pi/8)\,(\omega_{t\,e}\,\tau_{ee})^{\,-1}\,\nu_T^e(x)]}, \tag{67}$$

$$\nu_D^e = \frac{3\sqrt{\pi}}{4}\left[\left(1-\frac{1}{2\,x}\right)\psi(x)+\psi'(x)\right] + \frac{3\sqrt{\pi}}{4}\,Z_{\rm eff}, \tag{68}$$

$$\nu_\epsilon^e = \frac{3\sqrt{\pi}}{2}\left[\psi(x)-\psi'(x)\right], \tag{69}$$

$$\nu_T^e(x) = 3\,\nu_D^e(x) + \nu_\epsilon^e(x), \tag{70}$$

and

$$\psi(x) \;= \frac{2}{\sqrt{\pi}}\int_0^x \mathrm{e}^{-t^{\,2}}\,dt - \frac{2}{\sqrt{\pi}}\,x\,\mathrm{e}^{-x^{\,2}}, \tag{71}$$

$$\psi'(x) = \frac{2}{\sqrt{\pi}}\,x\,\mathrm{e}^{-x^{\,2}}. \tag{72}$$

Furthermore,

$$K_{ab}^i = g\,\frac{4}{3\sqrt{\pi}}\int_0^\infty \frac{e^{-x}\,x^{\,2+a+b}\,\nu_D^i(x)\,dx}{[x+\nu_{*\,i}\,\nu_D^i(x)]\,[x+(5\pi/8)\,(\omega_{t\,i}\,\tau_{ii})^{\,-1}\,\nu_T^i(x)]}, \tag{73}$$

$$\begin{aligned}\nu_D^i = {}& \frac{3\sqrt{\pi}}{4}\left[\left(1-\frac{1}{2\,x}\right)\psi(x)+\psi'(x)\right]\frac{1}{x} \\ & + \frac{3\sqrt{\pi}}{4}\,\alpha\left[\left(1-\frac{x_{iI}}{2\,x}\right)\psi\!\left(\frac{x}{x_{iI}}\right)+\psi'\!\left(\frac{x}{x_{iI}}\right)\right]\frac{1}{x},\end{aligned} \tag{74}$$

$$\begin{aligned}\nu_\epsilon^i = {}& \frac{3\sqrt{\pi}}{2}\left[\psi(x)-\psi'(x)\right]\frac{1}{x} \\ & + \frac{3\sqrt{\pi}}{2}\,\alpha\left[\frac{m_i}{m_I}\,\psi\!\left(\frac{x}{x_{iI}}\right)-\psi'\!\left(\frac{x}{x_{iI}}\right)\right]\frac{1}{x},\end{aligned}$$

$$\nu_T^i(x) = 3\,\nu_D^i(x) + \nu_\epsilon^i(x), \tag{75}$$

and, finally,

$$K_{ab}^I = g\,\frac{4}{3\sqrt{\pi}}\int_0^\infty \frac{e^{-x}\,x^{\,2+a+b}\,\nu_D^I(x)\,dx}{[x+\nu_{*\,I}\,\nu_D^I(x)]\,[x+(5\pi/8)\,(\omega_{t\,I}\,\tau_{II})^{\,-1}\,\nu_T^I(x)]}, \tag{76}$$

$$\begin{aligned}\nu_D^I = {}& \frac{3\sqrt{\pi}}{4}\left[\left(1-\frac{1}{2\,x}\right)\psi(x)+\psi'(x)\right]\frac{1}{x} \\ & + \frac{3\sqrt{\pi}}{4}\,\frac{1}{\alpha}\left[\left(1-\frac{x_{Ii}}{2\,x}\right)\psi\!\left(\frac{x}{x_{Ii}}\right)+\psi'\!\left(\frac{x}{x_{Ii}}\right)\right]\frac{1}{x},\end{aligned} \tag{77}$$

$$\nu_\epsilon^I = \frac{3\sqrt{\pi}}{2}\left[\psi(x)-\psi'(x)\right]\frac{1}{x}$$

$$+\frac{3\sqrt{\pi}}{2}\,\frac{1}{\alpha}\left[\frac{m_I}{m_i}\,\psi\!\left(\frac{x}{x_{Ii}}\right)-\psi'\!\left(\frac{x}{x_{Ii}}\right)\right]\frac{1}{x}, \tag{78}$$

$$\nu_T^I(x)=3\,\nu_D^I(x)+\nu_\epsilon^I(x). \tag{79}$$

Note that our expressions for the neoclassical viscosity matrices interpolate (in the most accurate manner possible) between the three standard neoclassical collisionality regimes (i.e., the banana, plateau, and Pfirsch-Schlüter regimes [33]).

3.5. Parallel Force and Heat Balance

Let

$$\tilde{\mu}^{\,I}=\alpha^{\,2}\,\frac{T_i}{T_I}\,x_{Ii}\,\mu^{\,I}. \tag{80}$$

The requirement of equilibrium force and heat balance parallel to the magnetic field [33, 34] leads us to define four 2×2 dimensionless ion matrices, $L^{\,ii}(\psi)$, $L^{\,iI}(\psi)$, $L^{\,Ii}(\psi)$, and $L^{\,II}(\psi)$, where,

$$\begin{pmatrix} L^{\,ii}, & L^{\,iI} \\ L^{\,Ii}, & L^{\,II} \end{pmatrix}=\begin{pmatrix} F^{\,ii}+\mu^{\,i}, & -F^{\,iI} \\ -F^{\,Ii}, & F^{\,II}+\tilde{\mu}^{\,I} \end{pmatrix}^{-1}\begin{pmatrix} F^{\,ii}, & -F^{\,iI} \\ -F^{\,Ii}, & F^{\,II} \end{pmatrix}. \tag{81}$$

and four 2×2 dimensionless electron matrices, $Q^{\,ee}(\psi)$, $L^{\,ee}(\psi)$, $L^{\,ei}(\psi)$, and $L^{\,eI}(\psi)$, where

$$Q^{\,ee}=(F^{\,ee}+\mu^{\,e})^{\,-1}, \tag{82}$$

$$L^{\,ee}=Q^{\,ee}\,F^{\,ee}, \tag{83}$$

$$L^{\,ei}=-\,Q^{\,ee}\left[F^{\,ei}\,(1-L^{\,ii})-F^{\,eI}\,L^{\,Ii}\right], \tag{84}$$

$$L^{\,eI}=-\,Q^{\,ee}\left[F^{\,eI}\,(1-L^{\,II})-F^{\,ei}\,L^{\,iI}\right]. \tag{85}$$

3.6. Neoclassical Ion Velocities

It is helpful to define the $\mathbf{E}\times\mathbf{B}$ frequency,

$$\omega_E(\psi)=-\frac{d\Phi}{d\psi}, \tag{86}$$

the species-a diamagnetic frequency,

$$\omega_{*\,a}(\psi)=-\frac{T_a}{e_a}\,\frac{d\ln p_a}{d\psi}, \tag{87}$$

and

$$\eta_a(\psi)=\frac{d\ln T_a}{d\ln n_a}. \tag{88}$$

Let $\mathbf{V}^{\,a}$ denote the fluid velocity of species-a. The equilibrium neoclassical poloidal and parallel fluid velocities of the two ion species are [33, 34]:

$$\frac{\mathbf{V}^{\,i}\cdot\nabla\theta}{\mathbf{B}\cdot\nabla\theta}\,\frac{\langle B^{\,2}\rangle}{I}=-L_{00}^{ii}\,\omega_{*\,i}+L_{01}^{ii}\left(\frac{\eta_i}{1+\eta_i}\right)\omega_{*\,i}-L_{00}^{iI}\,\omega_{*\,I}+L_{01}^{iI}\left(\frac{\eta_I}{1+\eta_I}\right)\omega_{*\,I}, \tag{89}$$

$$\frac{\mathbf{V}^{\,I}\cdot\nabla\theta}{\mathbf{B}\cdot\nabla\theta}\,\frac{\langle B^{\,2}\rangle}{I}=-L_{00}^{Ii}\,\omega_{*\,i}+L_{01}^{Ii}\left(\frac{\eta_i}{1+\eta_i}\right)\omega_{*\,i}-L_{00}^{II}\,\omega_{*\,I}+L_{01}^{II}\left(\frac{\eta_I}{1+\eta_I}\right)\omega_{*\,I}, \tag{90}$$

$$\frac{\langle\mathbf{V}^{\,i}\cdot\mathbf{B}\rangle}{I}=\omega_E+\omega_{*\,i}-L_{00}^{ii}\,\omega_{*\,i}+L_{01}^{ii}\left(\frac{\eta_i}{1+\eta_i}\right)\omega_{*\,i}-L_{00}^{iI}\,\omega_{*\,I}$$

$$+ L_{01}^{iI}\left(\frac{\eta_I}{1+\eta_I}\right)\omega_{*\,I}, \tag{91}$$

$$\frac{\langle \mathbf{V}^{\,I}\cdot\mathbf{B}\rangle}{I} = \omega_E + \omega_{*\,I} - L_{00}^{Ii}\,\omega_{*\,i} + L_{01}^{Ii}\left(\frac{\eta_i}{1+\eta_i}\right)\omega_{*\,i} - L_{00}^{II}\,\omega_{*\,I} + L_{01}^{II}\left(\frac{\eta_I}{1+\eta_I}\right)\omega_{*\,I}. \tag{92}$$

3.7. Parallel Current Density

The equilibrium parallel current density can be written

$$j_\parallel = j_{\rm bootstrap} + j_{\rm ohmic}, \tag{93}$$

where [33, 34]

$$\begin{aligned}\frac{\langle j_{\rm bootstrap}\,B\rangle}{I} = &-\left[1 - L_{00}^{ii} - \left(\frac{Z_{\rm eff}-1}{Z_I - Z_{\rm eff}}\right)L_{00}^{Ii} + \left(\frac{Z_I-1}{Z_I-Z_{\rm eff}}\right)L_{00}^{ei}\right]\frac{dp_i}{d\psi}\\ &-\left[L_{01}^{ii} + \left(\frac{Z_{\rm eff}-1}{Z_I - Z_{\rm eff}}\right)L_{01}^{Ii} - \left(\frac{Z_I-1}{Z_I-Z_{\rm eff}}\right)L_{01}^{ei}\right]n_i\,\frac{dT_i}{d\psi}\\ &-\left[1 - L_{00}^{II} - \left(\frac{Z_I - Z_{\rm eff}}{Z_{\rm eff}-1}\right)L_{00}^{iI} + \left(\frac{Z_I-1}{Z_{\rm eff}-1}\right)L_{00}^{eI}\right]\frac{dp_I}{d\psi}\\ &-\left[L_{01}^{II} + \left(\frac{Z_I - Z_{\rm eff}}{Z_{\rm eff}-1}\right)L_{01}^{iI} - \left(\frac{Z_I-1}{Z_{\rm eff}-1}\right)L_{01}^{eI}\right]n_I\,\frac{dT_I}{d\psi}\\ &-(1-L_{00}^{ee})\,\frac{dp_e}{d\psi} - L_{01}^{ee}\,n_e\,\frac{dT_e}{d\psi},\end{aligned} \tag{94}$$

and

$$\langle j_{\rm ohmic}\,B\rangle = Q_{00}^{ee}\,\sigma_{ee}\,\langle E_\parallel\,B\rangle, \tag{95}$$

with

$$\sigma_{ee} = \frac{n_e\,e^{\,2}\,\tau_{ee}}{m_e}. \tag{96}$$

4. Plasma Response to Resonant Magnetic Perturbation

4.1. Plasma Response

Consider the response of the plasma to a static RMP. Suppose that the RMP has $|m|$ periods in the poloidal direction, and $n > 0$ periods in the toroidal direction. (Note that m is positive if q is positive, and vice versa.) It is convenient to express the perturbed magnetic field in terms of the perturbed poloidal flux $\delta\psi(r,\theta,\phi,t)$:

$$\delta\mathbf{B} = \nabla\delta\psi\times R\,\nabla\phi, \tag{97}$$

where

$$\delta\psi(r,\theta,\phi,t) = \hat{\psi}(r,t)\,\exp[\,{\rm i}\,(m\,\theta - n\,\phi)]. \tag{98}$$

As is well known, the response of the plasma to the applied RMP is governed by the equations of perturbed, marginally-stable (i.e., $\partial/\partial t \equiv 0$), *ideal magnetohydrodynamics* (MHD) everywhere in the plasma, apart from a relatively narrow (in r) region in the vicinity of a resonant magnetic flux-surface at which

$\mathbf{B}\cdot\nabla\delta\psi = 0$ [22]. It follows from (4) that the resonant surface is located at $r = r_s$, where $q(r_s) = m/n$ [22].

It is convenient to parameterize the RMP in terms of the so-called perturbed *vacuum magnetic flux*, $\Psi_v(t) = |\Psi_v|\,\mathrm{e}^{-\mathrm{i}\,\varphi_v}$, which is defined to be the value of $\hat{\psi}(r,t)$ at $r = r_s$ in the presence of the RMP, but in the absence of the plasma. Here, φ_v is the helical phase of the RMP, and is assumed to be constant in time. Likewise, the response of the plasma in the vicinity of the resonant surface to the RMP is parameterized in terms of the so-called *reconnected magnetic flux*, $\Psi_s(t) = |\Psi_s|\,\mathrm{e}^{-\mathrm{i}\,\varphi_s}$, which is the actual value of $\hat{\psi}(r,t)$ at $r = r_s$. Here, $\varphi_s(t)$ is the helical phase of the reconnected flux.

The intrinsic stability of the m/n tearing mode is governed by the *tearing stability index* [36],

$$\Delta' = \left[\frac{d\ln\hat{\psi}}{dr}\right]_{r_s-}^{r_s+}, \tag{99}$$

where $\hat{\psi}(r)$ is a solution of the marginally-stable, ideal-MHD equations, for the case of an m/n helical perturbation, that satisfies physical boundary conditions at $r = 0$ and $r = a$ (in the absence of the RMP). According to resistive-MHD theory [36, 37], if $\Delta' > 0$ then the m/n tearing mode spontaneously reconnects magnetic flux at the resonant surface to form a helical magnetic island chain. In the following, it is assumed that $\Delta' < 0$, so that the m/n tearing mode is intrinsically stable. In this situation, any magnetic reconnection that takes place at the resonant surface is due solely to the RMP.

4.2. Nonlinear Response Regime

In the *nonlinear* local plasma response model adopted in this paper, the reconnected magnetic flux induced at the resonant surface by the RMP is governed by two equations. The first of these is the *Rutherford island width evolution equation* [37],

$$\mathcal{I}\,\tau_R\,\frac{d}{dt}\left(\frac{W}{r_s}\right) = \Delta'\,r_s + 2\,|m|\,\mathcal{A}\left(\frac{W_v}{W}\right)^2\cos\varphi, \tag{100}$$

where $\mathcal{I} = 0.8227$. Here,

$$\tau_R = \mu_0\left(r^2\,Q_{00}^{ee}\,\sigma_{ee}\right)_{r=r_s}, \tag{101}$$

is the resistive evolution timescale, and

$$W(t) = 4\left(\frac{|\Psi_s|}{s\,r_s\,|B_p(r_s)|}\right)^{1/2} r_s \tag{102}$$

the full (radial) width of the magnetic island chain that forms at the resonant surface. (In this paper, it is implicitly assumed that $W \ll a$.) Moreover, the neoclassical coefficient $Q_{00}^{ee}(r)$ is specified in Section 3.5, and

$$B_p \equiv \frac{\langle\mathbf{B}\cdot\nabla\Theta\rangle}{|\nabla\Theta|} = \frac{\epsilon\,B_0}{q\,\sqrt{1-\epsilon^2}} \tag{103}$$

is the equilibrium poloidal magnetic field. [See (17) and (21).] Note that (101) fully takes into account the modification of plasma parallel electrical conductivity due to the presence of impurity ions, as well as the modification due to trapped particles.

Moreover, (101) is valid in all three possible neoclassical collisionality regimes (i.e., banana, plateau, and Pfirsch-Schlüter [33]). Now,

$$W_v(t) = 4\left(\frac{|\Psi_v|}{s\, r_s\, |B_p(r_s)|}\right)^{1/2} r_s \tag{104}$$

is termed the vacuum island width. In addition, $s = (d\ln q/d\ln r)_{r=r_s}$ is the local magnetic shear, and $\mathcal{A}$ the amplification factor (i.e., the factor by which the radial magnetic field at the resonant surface due to the RMP is enhanced with respect to its vacuum value due to equilibrium plasma currents external to the resonant surface). Finally,

$$\varphi(t) = \varphi_s(t) - \varphi_v \tag{105}$$

is the helical phase of the island chain relative to the RMP.

The second governing equation is the so-called *no-slip constraint* [22],

$$\frac{d\varphi_s}{dt} - \omega = 0, \tag{106}$$

according to which the island chain is convected by the "plasma" (see the following sentence in parentheses) at the resonant surface. Here,

$$\varpi(t) = m\,\Omega_\theta(r_s,t) - n\,\Omega_\phi(r_s,t) \tag{107}$$

is the island phase velocity, and $\Omega_\theta(r,t)$ and $\Omega_\phi(r,t)$ are the plasma poloidal and toroidal angular velocity profiles, respectively. [To be more exact, $\Omega_\theta(r,t)$ and $\Omega_\phi(r,t)$ are the poloidal and toroidal angular velocity profiles of an imaginary fluid that convects reconnected magnetic flux at resonant surfaces. It is assumed that changes in these velocity profiles are mirrored by changes in the corresponding actual plasma velocity profiles. A magnetic island convected by the imaginary fluid propagates at its so-called natural phase velocity. The relationship between the natural phase velocity and the $\mathbf{E}\times\mathbf{B}$ frequency is specified in Section 4.4.]

The nonlinear response model adopted in this paper is valid as long as the width of the RMP-generated magnetic island chain at the resonant surface exceeds the linear layer width. This criterion is easily satisfied in present-day tokamaks, and will almost certainly be satisfied in ITER [24].

4.3. Plasma Angular Velocity Evolution

It is easily demonstrated that zero net electromagnetic torque can be exerted on magnetic flux surfaces located in a region of the plasma that is governed by the equations of marginally-stable, ideal-MHD [22]. Thus, any electromagnetic torque exerted on the plasma by the RMP develops in the immediate vicinity of the resonant surface, where ideal-MHD breaks down. The net poloidal and toroidal electromagnetic torques exerted in the vicinity of the resonant surface by the RMP take the forms [22, 23]

$$T_{\theta\,\mathrm{EM}} = -\frac{4\pi^2\,|m|\,m\,R_0}{\mu_0}\,\mathcal{A}\,|\Psi_v|\,|\Psi_s|\,\sin\varphi, \tag{108}$$

$$T_{\phi\,\mathrm{EM}} = \frac{4\pi^2\,|m|\,n\,R_0}{\mu_0}\,\mathcal{A}\,|\Psi_v|\,|\Psi_s|\,\sin\varphi, \tag{109}$$

respectively.

We can write

$$\Omega_\theta(r,t) = \Omega_{\theta\,0}(r) + \Delta\Omega_\theta(r,t), \tag{110}$$

$$\Omega_\phi(r,t) = \Omega_{\phi\,0}(r) + \Delta\Omega_\phi(r,t), \tag{111}$$

where $\Omega_{\theta\,0}(r)$ and $\Omega_{\phi\,0}(r)$ are the equilibrium poloidal and toroidal plasma angular velocity profiles, respectively, whereas $\Delta\Omega_\theta(r,t)$ and $\Delta\Omega_\phi(r,t)$ are the respective modifications to these profiles induced by the aforementioned electromagnetic torques. The modifications to the angular velocity profiles are governed by the poloidal and toroidal angular equations of motion of the plasma, which take the respective forms [22, 38]

$$4\pi^2 R_0 \left[(1+2\,q^2)\,\rho\,r^3\,\frac{\partial\Delta\Omega_\theta}{\partial t} - \frac{\partial}{\partial r}\left(\mu\,r^3\,\frac{\partial\Delta\Omega_\theta}{\partial r}\right) + \rho\,r^3\,\frac{\Delta\Omega_\theta}{\tau_\theta}\right] = T_{\theta\,\rm EM}\,\delta(r-r_s), \tag{112}$$

$$4\pi^2 R_0^3 \left[\rho\,r\,\frac{\partial\Delta\Omega_\phi}{\partial t} - \frac{\partial}{\partial r}\left(\mu\,r\,\frac{\partial\Delta\Omega_\phi}{\partial r}\right) + \rho\,r\,\frac{\Delta\Omega_\phi}{\tau_\phi}\right] = T_{\phi\,\rm EM}\,\delta(r-r_s), \tag{113}$$

and are subject to the spatial boundary conditions [22]

$$\frac{\partial\Delta\Omega_\theta(0,t)}{\partial r} = \frac{\partial\Delta\Omega_\phi(0,t)}{\partial r} = 0, \tag{114}$$

$$\Delta\Omega_\theta(a,t) = \Delta\Omega_\phi(a,t) = 0. \tag{115}$$

Here, $\mu(r)$ is the anomalous plasma perpendicular ion viscosity (due to plasma turbulence), whereas

$$\rho(r) \simeq m_i\,n_i + m_I\,n_I = \left\{m_i\left(\frac{Z_I - Z_{\rm eff}}{Z_I - 1}\right) + m_I\left[\frac{Z_{\rm eff}-1}{Z_I\,(Z_I-1)}\right]\right\} n_e \tag{116}$$

is the plasma mass density. [See (29) and (30).] Furthermore

$$\frac{1}{\tau_\theta(r)} = \left(\frac{B_0}{B_p}\right)^2 \frac{\mu_{00}^i}{\tau_{ii}} = \left(\frac{q\,\sqrt{1-\epsilon^2}}{\epsilon}\right)^2 \frac{\mu_{00}^i}{\tau_{ii}} \tag{117}$$

is the neoclassical poloidal flow-damping rate [34, 39]. [See (103).] Here, the neoclassical coefficient $\mu_{00}^i(r)$ is specified in Section 3.4. Note that the previous expression is valid in all possible neoclassical collisionality regimes (i.e., banana, plateau, and Pfirsch-Schlüter [33]), and also fully takes into account the presence of impurity ions. Finally, $1/\tau_\phi(r)$ is the neoclassical toroidal flow-damping rate. The neoclassical toroidal flow-damping is assumed to be generated by non-resonant components of the applied RMP [40, 41].

The factor $(1+2\,q^2)$ in (112) derives from the fact that incompressible poloidal flow has a poloidally-varying toroidal component that effectively increases the plasma mass being accelerated by the poloidal flow-damping force [38].

It turns out that, in the presence of poloidal and toroidal flow-damping, the modifications to the plasma poloidal and toroidal angular velocity profiles are radially localized in the vicinity of the resonant surface [41]. Assuming that this is the case, it is a good approximation to replace $q(r)$, $\rho(r)$, $\mu(r)$, $\tau_\theta(r)$, and $\tau_\phi(r)$ in (112) and (113) by their values at the resonant surface. We are, nevertheless, assuming that the localization width greatly exceeds the width of the magnetic island chain.

Equations (107), (110), and (111) imply that

$$\varpi(t) = \varpi_0 + m\,\Delta\Omega_\theta(r_s,t) - n\,\Delta\Omega_\phi(r_s,t), \tag{118}$$

where

$$\varpi_0 = m\,\Omega_{\theta\,0}(r_s) - n\,\Omega_{\phi\,0}(r_s) \tag{119}$$

is the so-called *natural phase velocity* of the m/n tearing mode [22]. In other words, ϖ_0 is the helical phase velocity of a naturally unstable m/n tearing mode in the absence of the RMP.

4.4. Natural Phase Velocity

It turns out that the natural phase velocity of a nonlinear magnetic island chain in a conventional tokamak plasma is predominately determined by the neoclassical parallel ion viscous stress tensor. According to the analysis of [28],

$$\varpi_0 = -n\left\langle\frac{V_\phi^{\,i}}{R}\right\rangle_{r=r_s} \simeq -n\left(\frac{\langle\mathbf{V}^{\,i}\cdot\mathbf{B}\rangle}{I}\right)_{r=r_s}. \tag{120}$$

In other words, the island chain is effectively convected by the toroidal component of the equilibrium neoclassical majority ion flow at the resonant surface, but not by the poloidal component. It follows from (91) that

$$\varpi_0 = -n\left(\omega_E + \left[1 - L_{00}^{ii} + L_{01}^{ii}\left(\frac{\eta_i}{1+\eta_i}\right)\right]\omega_{*\,i} - \left[L_{00}^{iI} - L_{01}^{iI}\left(\frac{\eta_I}{1+\eta_I}\right)\right]\omega_{*\,I}\right)_{r=r_s}. \tag{121}$$

Here, the neoclassical coefficients $L_{00}^{ii}(r)$, $L_{01}^{ii}(r)$, $L_{00}^{iI}(r)$, and $L_{01}^{iI}(r)$ are specified in Section 3.5. Note that the previous expression is valid in all possible neoclassical collisionality regimes (i.e., banana, plateau, and Pfirsch-Schlüter [33]), and also fully takes into account the presence of impurity ions.

Incidentally, according to linear theory [30], the natural phase velocity is

$$\varpi_{\perp\,e} = -n\,(\omega_E + \omega_{*\,e})_{r=r_s}, \tag{122}$$

which is equivalent to saying that the island chain is convected by the electron fluid.

4.5. Unnormalized Nonlinear Plasma Response Model

Our nonlinear plasma response model reduces to the following closed set of equations [24]:

$$\mathcal{I}\,\tau_R\,\frac{d}{dt}\left(\frac{W}{r_s}\right) = \Delta'\,r_s + 2\,|m|\,\mathcal{A}\left(\frac{W_v}{W}\right)^2\cos\varphi, \tag{123}$$

$$\frac{d\varphi}{dt} = \varpi, \tag{124}$$

$$\varpi = \varpi_0 + m\,\Delta\Omega_\theta(r_s,t) - n\,\Delta\Omega_\phi(r_s,t), \tag{125}$$

$$\left[(1+2\,q_s^2)\,\rho_s\,r^3\,\frac{\partial\Delta\Omega_\theta}{\partial t} - \frac{\partial}{\partial r}\left(\mu_s\,r^3\,\frac{\partial\Delta\Omega_\theta}{\partial r}\right) + \rho_s\,r^3\,\frac{\Delta\Omega_\theta}{\tau_{\theta\,s}}\right] = -\frac{|m|\,m}{\mu_0}\,\mathcal{A}\left(\frac{W_v}{4\,r_s}\right)^2\left(\frac{W}{4\,r_s}\right)^2\left[s\,r_s\,B_p(r_s)\right]^2\sin\varphi\,\delta(r-r_s), \tag{126}$$

$$R_0^2\left[\rho_s\,r\,\frac{\partial\Delta\Omega_\phi}{\partial t} - \frac{\partial}{\partial r}\left(\mu_s\,r\,\frac{\partial\Delta\Omega_\phi}{\partial r}\right) + \rho_s\,r\,\frac{\Delta\Omega_\phi}{\tau_{\phi\,s}}\right]$$

$$= \frac{|m|\, n}{\mu_0}\, \mathcal{A} \left(\frac{W_v}{4\, r_s}\right)^2 \left(\frac{W}{4\, r_s}\right)^2 \left[s\, r_s\, B_p(r_s)\right]^2 \sin\varphi\, \delta(r - r_s), \quad (127)$$

$$\frac{\partial \Delta\Omega_\theta(0,t)}{\partial r} = \frac{\partial \Delta\Omega_\phi(0,t)}{\partial r} = 0, \quad (128)$$

$$\Delta\Omega_\theta(a,t) = \Delta\Omega_\phi(a,t) = 0. \quad (129)$$

Here, $q_s = q(r_s) = m/n$, $\rho_s = \rho(r_s)$, $\mu_s = \mu(r_s)$, $\tau_{\theta\, s} = \tau_\theta(r_s)$, and $\tau_{\phi\, s} = \tau_\phi(r_s)$.

4.6. Normalized Nonlinear Plasma Response Model

For the sake of simplicity, we shall assume that the quantities $\mathcal{A}$ and $\Delta'\, r_s$ take their vacuum values, 1 and $-2\,|m|$, respectively. (The former assumption is equivalent to assuming that there is negligible equilibrium plasma current external to the resonant surface.) The hydromagnetic and momentum confinement timescales are defined

$$\tau_H = \frac{R_0}{|B_0|}\, \frac{\sqrt{\mu_0\, \rho(r_s)\, (1 - \epsilon_s^2)}}{n\, s}, \quad (130)$$

$$\tau_M = \frac{a^2\, \rho_s}{\mu_s}, \quad (131)$$

respectively, where $\epsilon_s = \epsilon(r_s) = r_s/R_0$. It is convenient to adopt the following normalization scheme: $\hat{t} = t/\tau_H$, $\hat{r} = r/a$, $\hat{r}_s = r_s/a$, $\hat{\varpi} = \varpi\, \tau_H$, $\hat{\varpi}_0 = \varpi_0\, \tau_H$, $\hat{\varpi}_\theta = -m\, \Delta\Omega_\theta\, \tau_H$, $\hat{\varpi}_\phi = n\, \Delta\Omega_\phi\, \tau_H$, $\hat{W} = W/W_v$, $\hat{\tau}_M = \tau_M/\tau_H$, $\hat{\tau}_\theta = \tau_{\theta\, s}/\tau_H$, and $\hat{\tau}_\phi = \tau_{\phi\, s}/\tau_H$. The normalized versions of (123)–(129) are:

$$\frac{\mathcal{I}\, S\, W_v}{2\, |m|\, r_s}\, \frac{d\hat{W}}{d\hat{t}} = -1 + \frac{\cos\varphi}{\hat{W}^2}, \quad (132)$$

$$\frac{d\varphi}{d\hat{t}} = \hat{\varpi}, \quad (133)$$

$$\hat{\varpi} = \hat{\varpi}_0 - \hat{\varpi}_\theta(\hat{r}_s, \hat{t}) - \hat{\varpi}_\phi(\hat{r}_s, \hat{t}), \quad (134)$$

$$(1 + 2\, q_s^2)\, \hat{r}^3\, \frac{\partial \hat{\varpi}_\theta}{\partial \hat{t}} - \frac{1}{\hat{\tau}_M}\, \frac{\partial}{\partial \hat{r}} \left(\hat{r}^3\, \frac{\partial \hat{\varpi}_\theta}{\partial \hat{r}}\right) + \frac{1}{\hat{\tau}_\theta}\, \hat{r}^3\, \hat{\varpi}_\theta$$

$$= |m| \left(\frac{W_v}{4\, a}\right)^4 \hat{W}^2\, \sin\varphi\, \delta(\hat{r} - \hat{r}_s), \quad (135)$$

$$\hat{r}\, \frac{\partial \hat{\varpi}_\phi}{\partial \hat{t}} - \frac{1}{\hat{\tau}_M}\, \frac{\partial}{\partial \hat{r}} \left(\hat{r}\, \frac{\partial \hat{\varpi}_\phi}{\partial \hat{r}}\right) + \frac{1}{\hat{\tau}_\phi}\, \hat{r}\, \hat{\varpi}_\phi = \zeta\, |m| \left(\frac{W_v}{4\, a}\right)^4 \hat{W}^2\, \sin\varphi\, \delta(\hat{r} - \hat{r}_s), \quad (136)$$

$$\frac{\partial \hat{\varpi}_\theta(0,\hat{t})}{\partial \hat{r}} = \frac{\partial \hat{\varpi}_\phi(0,\hat{t})}{\partial \hat{r}} = 0, \quad (137)$$

$$\hat{\varpi}_\theta(1,\hat{t}) = \hat{\varpi}_\phi(1,\hat{t}) = 0, \quad (138)$$

where

$$S = \frac{\tau_R}{\tau_H}, \quad (139)$$

$$\zeta = \left(\frac{a}{R_0\, q_s}\right)^2. \quad (140)$$

5. Pulsating Magnetic Island Chains

5.1. Cycle-Averaged Nonlinear Plasma Response Model

As is described in [23] and [28, 26, 27], a non-stationary solution of (132)–(138) (i.e., a solution in which the magnetic island chain driven at the resonant surface does not have a fixed phase relation with respect to the RMP) is characterized by an island chain whose helical phase continually increases (assuming, for the sake of definiteness, that $\hat{\varpi} > 0$) in time, and whose width *pulsates*, periodically falling to zero, at which times its helical phase jumps by $-\pi$ radians. Suppose that the island chain is born (at zero width) at helical phase φ_0, attains its maximum width at helical phase $\varphi_0 + \pi/2$, and disappears at helical phase $\varphi_0 + \pi$, at which time its helical phase jumps back to φ_0, and the cycle repeats. It is helpful to define the cycle-average operator [26]:

$$\langle \cdots \rangle_\varphi = \frac{1}{\pi} \int_{\varphi_0}^{\varphi_0+\pi} (\cdots)\, d\varphi. \tag{141}$$

Equations (132) and (133) can be combined to give

$$\lambda \frac{du}{d\varphi} \simeq \cos\varphi - u^{\,2/3}, \tag{142}$$

where

$$u = \hat{W}^{\,3}, \tag{143}$$

$$\lambda = \frac{\langle \hat{\varpi} \rangle_\varphi \mathcal{I}\, S\, W_v}{6\,|m|\, r_s}. \tag{144}$$

Let

$$T \equiv \hat{W}^{\,2} \sin\varphi = u^{\,2/3} \sin\varphi. \tag{145}$$

According to the analysis of [26], (142) possesses pulsating solutions characterized by

$$\frac{\langle \varphi \rangle_\varphi}{\pi} \simeq \frac{\lambda^{\,2}}{1 + 2\,\lambda^{\,2}} - \frac{0.1756\,\lambda^{\,2}}{1 + 0.4950\,|\lambda|^{\,8/3}}, \tag{146}$$

$$\langle \hat{W}^{\,4} \rangle_\varphi \simeq \frac{0.5}{1 + 0.8624\,|\lambda|^{\,4/3}}, \tag{147}$$

$$\langle T \rangle_\varphi \simeq \frac{0.4577\,\lambda}{1 + 0.8546\,|\lambda|^{\,5/3}}. \tag{148}$$

Finally, the cycle average of (134)–(138) yields

$$\langle \hat{\varpi} \rangle_\varphi = \hat{\varpi}_0 - \langle \hat{\varpi}_\theta \rangle_\varphi(\hat{r}_s) - \langle \hat{\varpi}_\phi \rangle_\varphi(\hat{r}_s), \tag{149}$$

$$-\frac{1}{\hat{\tau}_M} \frac{d}{d\hat{r}} \left(\hat{r}^{\,3} \frac{d\langle \hat{\varpi}_\theta \rangle_\varphi}{d\hat{r}} \right) + \frac{1}{\hat{\tau}_\theta}\, \hat{r}^{\,3}\, \langle \hat{\varpi}_\theta \rangle_\varphi = |m| \left(\frac{W_v}{4\,a} \right)^4 \langle T \rangle_\varphi\, \delta(\hat{r} - \hat{r}_s), \tag{150}$$

$$-\frac{1}{\hat{\tau}_M} \frac{d}{d\hat{r}} \left(\hat{r} \frac{d\langle \hat{\varpi}_\phi \rangle_\varphi}{d\hat{r}} \right) + \frac{1}{\hat{\tau}_\phi}\, \hat{r}\, \langle \hat{\varpi}_\phi \rangle_\varphi = \zeta\, |m| \left(\frac{W_v}{4\,a} \right)^4 \langle T \rangle_\varphi\, \delta(\hat{r} - \hat{r}_s), \tag{151}$$

$$\frac{d\langle \hat{\varpi}_\theta \rangle_\varphi(0)}{d\hat{r}} = \frac{d\langle \hat{\varpi}_\phi \rangle_\varphi(0)}{d\hat{r}} = 0, \tag{152}$$

$$\langle \hat{\varpi}_\theta \rangle_\varphi(1) = \langle \hat{\varpi}_\phi \rangle_\varphi(1) = 0. \tag{153}$$

5.2. Solution of Cycle-Averaged Plasma Angular Equations of Motion

Let [42]

$$\langle \hat{\varpi}_\theta \rangle_\varphi(\hat{r}) = \sum_{n=1,N} a_n \frac{y_n(\hat{r})}{y_n(\hat{r}_s)}, \tag{154}$$

$$\langle \hat{\varpi}_\phi \rangle_\varphi(\hat{r}) = \sum_{n=1,N} b_n \frac{z_n(\hat{r})}{z_n(\hat{r}_s)}, \tag{155}$$

where

$$y_n(\hat{r}) = \frac{J_1(j_{1,n}\,\hat{r})}{\hat{r}}, \tag{156}$$

$$z_n(\hat{r}) = J_0(j_{0,n}\,\hat{r}). \tag{157}$$

Here, $J_m(z)$ is a standard Bessel function, and $j_{m,n}$ denotes the nth zero of the $J_m(z)$ Bessel function [43]. Note that (154) and (155) automatically satisfy the boundary conditions (152) and (153), and are complete in the limit $N \to \infty$.

It is easily demonstrated that [43]

$$\frac{d}{d\hat{r}}\left(\hat{r}^{\,3}\,\frac{dy_n}{d\hat{r}}\right) = -\,j_{1,n}^2\,\hat{r}^{\,3}\,y_n, \tag{158}$$

$$\frac{d}{d\hat{r}}\left(\hat{r}\,\frac{dz_n}{d\hat{r}}\right) = -\,j_{0,n}^2\,\hat{r}\,z_n, \tag{159}$$

and [44]

$$\int_0^1 \hat{r}^{\,3}\,y_n(\hat{r})\,y_m(\hat{r})\,d\hat{r} = \frac{1}{2}\,[J_2(j_{1,n})]^{\,2}\,\delta_{nm}, \tag{160}$$

$$\int_0^1 \hat{r}\,z_n(\hat{r})\,z_m(\hat{r})\,d\hat{r} = \frac{1}{2}\,[J_1(j_{0,n})]^{\,2}\,\delta_{nm} \tag{161}$$

Thus, (149)–(151) and (154)–(161) yield

$$\langle \hat{\varpi} \rangle_\varphi = \hat{\varpi}_0 - \sum_{n=1,N} a_n - \sum_{n=1,N} b_n, \tag{162}$$

where

$$a_n = \frac{\alpha_n}{1/\hat{\tau}_\theta + j_{1,n}^2/\hat{\tau}_M}\,|m|\left(\frac{W_v}{4\,a}\right)^4\,\langle T\rangle_\varphi, \tag{163}$$

$$b_n = \frac{\zeta\,\beta_n}{1/\hat{\tau}_\phi + j_{0,n}^2/\hat{\tau}_M}\,|m|\left(\frac{W_v}{4\,a}\right)^4\,\langle T\rangle_\varphi, \tag{164}$$

and

$$\alpha_n = \left[\frac{\sqrt{2}\,J_1(j_{1,n}\,\hat{r}_s)}{\hat{r}_s\,J_2(j_{1,n})}\right]^2, \tag{165}$$

$$\beta_n = \left[\frac{\sqrt{2}\,J_0(j_{0,n}\,\hat{r}_s)}{J_1(j_{0,n})}\right]^2. \tag{166}$$

5.3. Cycle-Averaged Torque Balance

Let

$$x = \frac{\langle \hat{\varpi} \rangle_\varphi}{\hat{\varpi}_0}. \tag{167}$$

Equations (144), (148), and (162)–(166) can be combined to give the following cycle-averaged torque balance equation [26]:

$$g(x) = 0, \tag{168}$$

where

$$g(x) \equiv \gamma\, x^{\,8/3} - \gamma\, x^{\,5/3} + \frac{\beta}{2\cdot 2^{\,1/3}}\, x - \frac{1}{2^{\,5}\cdot 2^{\,1/3}}, \tag{169}$$

and

$$\beta = \frac{1}{2^{\,4}} + \mathcal{K}\,(\mathcal{J}\,\Sigma)\left(\frac{\mathcal{I}\,S}{3}\right)\left(\frac{r_s}{a}\right)^4\left(\frac{W_v}{r_s}\right)^5, \tag{170}$$

$$\gamma = \mathcal{K}\left(\frac{|\hat{\varpi}_0|}{|m|}\right)^{5/3}\left(\frac{\mathcal{I}\,S}{3}\right)^{5/3}\left(\frac{W_v}{r_s}\right)^{5/3}, \tag{171}$$

with

$$\mathcal{J} = \frac{0.5356}{2^{\,6}}, \tag{172}$$

$$\mathcal{K} = \frac{0.8543}{2^{\,7}}, \tag{173}$$

$$\Sigma = \sum_{n=1,N}\left(\frac{\alpha_n}{1/\hat{\tau}_\theta + j_{1,n}^2/\hat{\tau}_M} + \frac{\zeta\,\beta_n}{1/\hat{\tau}_\phi + j_{0,n}^2/\hat{\tau}_M}\right). \tag{174}$$

Let

$$\frac{W_c}{r_s} = \frac{(1-1/2^{\,4})^{1/5}}{\mathcal{K}^{\,1/5}\,(\mathcal{J}\,\Sigma)^{\,1/5}\,(\mathcal{I}\,S/3)^{1/5}\,(r_s/a)^{4/5}}, \tag{175}$$

$$\frac{\hat{\varpi}_c}{|m|} = \frac{(\mathcal{J}\,\Sigma)^{\,1/5}\,(r_s/a)^{4/5}}{(1-1/2^{\,4})^{1/5}\,\mathcal{K}^{\,2/5}\,(\mathcal{I}S/3)^{4/5}}. \tag{176}$$

It follows that

$$\beta = \frac{1}{2^{\,4}} + \left(1 - \frac{1}{2^{\,4}}\right)\left(\frac{W_v}{W_c}\right)^5, \tag{177}$$

$$\gamma = \left(\frac{W_v}{W_c}\right)^{5/3}\left(\frac{|\hat{\varpi}_0|}{\hat{\varpi}_c}\right)^{5/3}. \tag{178}$$

Here, x parameterizes the actual (i.e., in the presence of the RMP) plasma rotation at the resonant surface, β parameterizes the amplitude of the RMP, and γ parameterizes the intrinsic (i.e., in the absence of the RMP) plasma rotation at the resonant surface.

The numerical solution of the cycle-averaged torque balance equation, (168), is shown in Figure 1 (upper panel). The solution exhibits a forbidden band of plasma rotation frequencies when $\gamma > 1$ (i.e., when the intrinsic plasma rotation is sufficiently high). This band separates a branch of dynamically stable, low-rotation solutions from a branch of dynamically stable, high-rotation solutions. If a low-rotation solution crosses the lower boundary of the forbidden band then a bifurcation to a high-rotation

solution is triggered. Likewise, if a high-rotation solution crosses the upper boundary of the forbidden band then a bifurcation to a low-rotation solution is triggered.

It is helpful to define the cycle-averaged shielding factor,

$$\mathcal{S} = \frac{1}{(\langle \hat{W}^{\,4}\rangle_\varphi)^{\,1/2}}. \tag{179}$$

This quantity represents the mean factor by which the reconnected magnetic flux driven at the resonant surface is reduced by plasma rotation, relative to its value in the absence of plasma rotation. Figure 1 (lower panel) shows the shielding factor for solutions of the cycle-averaged torque balance equation that lie on the boundary of the forbidden band of plasma rotation frequencies (i.e., they lie on the thick curve in the upper panel of Figure 1). It can be seen that low-rotation solutions are characterized by weak shielding [i.e., $\mathcal{S} \sim \mathcal{O}(1)$], whereas high-rotation solutions are characterized by strong shielding (i.e., $\mathcal{S} \gg 1$). Hence, high-rotation to low-rotation bifurcations are associated with the sudden breakdown of strong shielding, whereas low-rotation to high-rotation bifurcations are characterized by the sudden onset of strong shielding.

To a good approximation, the bifurcation from the high-rotation to the low-rotation solution branch occurs when β exceeds the critical value [26]

$$\beta_+ \simeq 1 + \frac{12}{5^{\,5/3}}\,(\gamma - 1), \tag{180}$$

whereas the bifurcation from the low-rotation to the high-rotation solution branch occurs when β falls below the critical value [26]

$$\beta_- \simeq 1 + \frac{5}{2\,(54)^{\,1/5}}\,(\gamma^{\,3/5} - 1). \tag{181}$$

The previous two expressions are only valid when $|\hat{\varpi}_0| > \hat{\varpi}_c$ (i.e, when $\gamma > 1$). For $|\hat{\varpi}_0| \leq \hat{\varpi}_c$, there is no forbidden band of plasma rotation frequencies, and, consequently, there are no bifurcations.

Let the bifurcation from the high-rotation to the low-rotation solution branch occur when the vacuum island width exceeds the critical value $W_{v\,+}$. Furthermore, let

$$y_+ = \left(\frac{W_{v+}}{W_c}\right)^{5/3}. \tag{182}$$

It follows from (177), (178), and (180) that y_+ is the most positive real root of

$$\left(1 - \frac{1}{2^{\,4}}\right) y_+^3 - \frac{12}{5^{\,5/3}}\left(\frac{|\hat{\varpi}_0|}{\hat{\varpi}_c}\right)^{5/3} y_+ + \frac{12}{5^{\,5/3}} - \left(1 - \frac{1}{2^{\,4}}\right) = 0. \tag{183}$$

Likewise, let the bifurcation from the low-rotation to the high-rotation solution branch occur when the vacuum island width falls below the critical value W_{v-}. Furthermore, let

$$y_- = \left(\frac{W_{v-}}{W_c}\right)^{5}. \tag{184}$$

It follows that y_- is the most positive real root of

$$\left(1 - \frac{1}{2^{\,4}}\right) y_-^5 - \frac{5}{2\,(54)^{\,1/5}}\left(\frac{|\hat{\varpi}_0|}{\hat{\varpi}_c}\right) y_- + \frac{5}{2\,(54)^{\,1/5}} - \left(1 - \frac{1}{2^{\,4}}\right) = 0. \tag{185}$$

Finally, let b_v be the m/n component of the vacuum radial magnetic field due to the RMP at $r = a$. The bifurcation from the high-rotation to the low-rotation solution branch occurs when b_v exceeds the critical value $b_{v\,+}$, where

$$\frac{b_{v\,+}}{|B_0|} = \frac{(n\,s)\,(a/R_0)\,y_+^{6/5}}{2^{\,4}\,(r_s/a)^{\,|m|-2}\,\sqrt{1-\epsilon_s^2}}\left(\frac{W_c}{r_s}\right)^2. \tag{186}$$

[See (97), (103), and (104).] (Here, we are again assuming that there is negligible equilibrium plasma current external to the resonant surface.) Likewise, the bifurcation from the low-rotation to the high-rotation solution branch occurs when b_v falls below the critical value $b_{v\,-}$, where

$$\frac{b_{v\,-}}{|B_0|} = \frac{(n\,s)\,(a/R_0)\,y_-^{2/5}}{2^{\,4}\,(r_s/a)^{\,|m|-2}\,\sqrt{1-\epsilon_s^2}}\left(\frac{W_c}{r_s}\right)^2. \tag{187}$$

6. Locked Magnetic Island Chains

6.1. Steady-State Torque Balance

A locked solution of (132)–(138) (i.e., a solution in which the magnetic island chain driven at the resonant surface has a fixed phase relation with respect to the RMP) is characterized by an island chain whose width and helical phase are constant in time. The steady-state (i.e., $\partial/\partial\hat{t} = 0$) versions of (132)–(138) are:

$$\hat{W} = \cos^{1/2}\varphi, \tag{188}$$

$$0 = \hat{\varpi}_0 - \hat{\varpi}_\theta(\hat{r}_s) - \hat{\varpi}_\phi(\hat{r}_s), \tag{189}$$

$$-\frac{1}{\hat{\tau}_M}\frac{d}{d\hat{r}}\left(\hat{r}^{\,3}\,\frac{d\hat{\varpi}_\theta}{d\hat{r}}\right) + \frac{1}{\hat{\tau}_\theta}\,\hat{r}^{\,3}\,\hat{\varpi}_\theta = |m|\left(\frac{W_v}{4\,a}\right)^4\,\hat{W}^{\,2}\,\sin\varphi\,\delta(\hat{r}-\hat{r}_s), \tag{190}$$

$$\frac{1}{\hat{\tau}_M}\frac{d}{d\hat{r}}\left(\hat{r}\,\frac{d\hat{\varpi}_\phi}{d\hat{r}}\right) + \frac{1}{\hat{\tau}_\phi}\,\hat{r}\,\hat{\varpi}_\phi = \zeta\,|m|\left(\frac{W_v}{4\,a}\right)^4\,\hat{W}^{\,2}\,\sin\varphi\,\delta(\hat{r}-\hat{r}_s), \tag{191}$$

$$\frac{d\hat{\varpi}_\theta(0)}{d\hat{r}} = \frac{d\hat{\varpi}_\phi(0)}{d\hat{r}} = 0, \tag{192}$$

$$\hat{\varpi}_\theta(1) = \hat{\varpi}_\phi(1) = 0. \tag{193}$$

Making use of the representation (154)–(157), we arrive at the following steady-state torque balance equation:

$$\frac{\hat{\varpi}_0}{|m|} = \frac{\Sigma}{2^{\,9}}\left(\frac{r_s}{a}\right)^4\left(\frac{W_v}{r_s}\right)^4\sin 2\varphi. \tag{194}$$

Clearly, there is a bifurcation from the locked to the pulsating solution branch when $|\varphi|$ exceeds the critical value $\pi/4$, which corresponds to W_v falling below the critical value $W_{v\,0}$, where

$$\left(\frac{W_{v\,0}}{r_s}\right)^2 = \frac{2^{\,9/2}\,(|\hat{\varpi}_0|/|m|)^{\,1/2}}{\Sigma^{\,1/2}\,(r_s/a)^{\,2}}. \tag{195}$$

Note, from (188), that the locked solution branch (for which $|\varphi| < \pi/4$) is not characterized by strong shielding [i.e., $\hat{W} \sim \mathcal{O}(1)$]. The bifurcation from the locked to the pulsating solution branch occurs when b_v falls below the critical value $b_{v\,0}$, where

$$\frac{b_{v\,0}}{|B_0|} = \frac{(n\,s)\,(a/R_0)}{2^{\,4}\,(r_s/a)^{\,|m|-2}\,\sqrt{1-\epsilon_s^2}}\left(\frac{W_{v\,0}}{r_s}\right)^2. \tag{196}$$

6.2. Mode Penetration and Mode Unlocking Thresholds

In most circumstances, $b_{v\,+} > b_{v\,0} > b_{v\,-}$, which implies that if b_v exceeds the critical value $b_{v\,\rm pen} = b_{v\,+}$ then there is a bifurcation from the strongly-shielded, high-rotation, pulsating solution branch to the weakly-shielded, locked solution branch. Moreover, if b_v falls below the critical value $b_{v\,\rm ulk} = b_{v\,0}$ then there is a bifurcation from the weakly-shielded, locked solution branch to the strongly-shielded, high-rotation, pulsating solution branch. In a relatively small number of cases, $b_{v\,+} > b_{v\,-} > b_{v\,0}$, which implies that if b_v exceeds the critical value $b_{v\,\rm pen} = b_{v\,+}$ then there is a bifurcation from the strongly-shielded, high-rotation, pulsating solution branch to the weakly-shielded, low-rotation, pulsating solution branch. Moreover, if b_v falls below the critical value $b_{v\,\rm ulk} = b_{v\,-}$ then there is a bifurcation from the weakly-shielded, low-rotation, pulsating solution branch to the strongly-shielded, high-rotation, pulsating solution branch. Finally, if $|\hat{\varpi}_0| < \hat{\varpi}_c$ then $b_{v\,\rm pen} = b_{v\,\rm ulk} = b_{v\,0}$. In this case, there is a smooth transition from the pulsating solution branch to the locked solution branch when b_v exceeds the critical value $b_{v\,\rm pen}$, and a smooth transition from the locked solution branch to the pulsating solution branch when b_v falls below the same critical value.

7. Application to DIII-D H-Mode Discharges

7.1. DIII-D Discharge #158115

Following [18] and [24], this paper concentrates on a particular (but completely typical) DIII-D H-mode discharge (#158115) [16] in which ELMs were successfully suppressed by an externally applied $n = 2$ RMP. The electron number density, electron temperature, safety-factor, and $\mathbf{E}\times\mathbf{B}$ frequency profiles in the pedestal region of this discharge are shown in Figure 2 at a particular instance in time (3399 ms) at which the influence of the applied RMP on these profiles is negligible. Note that, in this paper, the flux-surface label r is identified with the flux-surface averaged minor radius. The remaining parameters that characterize the discharge are $B_0 = -1.94\,\rm T$, $R_0 = 1.75\,\rm m$, $a = 0.93\,\rm m$, $Z_{\rm eff} = 2.5$, $M_i = 2$, $M_I = 12.011$ (which corresponds to a deuterium plasma with carbon impurity ions), and $\chi_\perp \equiv \rho_s/\mu_s = 1\,\rm m^2/s$. Note that, in the following, the majority ion, impurity ion, and electron temperatures are all assumed to be equal, and toroidal flow-damping is neglected. According to [18], the density pump-out is due to a locked magnetic island chain driven at the $m = -11/n = 2$ resonant surface, which lies at the bottom of the pedestal. Furthermore, ELM suppression is due to mode penetration at the $m = -8/n = 2$ resonant surface, which lies at the top of the pedestal.

7.2. Edge Safety-Factor Scan

The most striking observed feature of RMP-induced ELM suppression in an H-mode tokamak discharge is that it only occurs when q_{95} takes values that lie in certain narrow windows [15, 16]. In order to gain a better understanding of this phenomenon, we shall crudely simulate a q_{95}-scan in DIII-D discharge #158115 by taking the profiles shown in Figure 2 and adding a constant offset to the safety-factor: i.e.,

$$q(r) \rightarrow q(r) + \Delta q. \tag{197}$$

The unmodified equilibrium is characterized by $q_{95} = -4.34$. Varying the constant offset, Δq, allows us to change q_{95}, while keeping the density, temperature, and

rotation profiles constant. Moreover, by varying q_{95}, it is possible to move a given resonant surface all the way though the pedestal region.

Figure 3 specifies how the natural phase velocity, ϖ_0 [see (121)], at the $m = -8/n = 2$ resonant surface depends on q_{95}. For comparison, the figure shows the natural phase velocity predicted by linear theory, $\varpi_{\perp\, e} \equiv -n\,(\omega_E + \omega_{*\, e})_{r=r_s}$. It is clear that $\varpi_0 < \varpi_{\perp\, e}$. In other words, as expected, the nonlinear natural phase velocity is offset from the linear natural phase velocity in the ion diamagnetic (i.e., negative) direction. In addition, Figure 3 specifies how the mode penetration and unlocking thresholds at the $m = -8/n = 2$ resonant surface, as well as the corresponding shielding factors just before mode penetration and unlocking, depend on q_{95}.

According to Figure 3, the plasma response at the $-8/2$ resonant surface is characterized by strong shielding just prior to mode penetration (i.e., $\mathcal{S} \gg 1$) and a large penetration threshold (i.e., $b_{v\,\rm pen} \gg 10\,\rm G$) for all values of $-q_{95}$ in the range $-q_{95} > 3.8$, except for a narrow window of values centered at $-q_{95} = 4.55$. It should be noted that in DIII-D discharges the maximum practical amplitude of the vacuum radial magnetic field at the plasma boundary, b_v, for a particular helical harmonic of an applied $n = 2$ RMP, is typically about 10 G [18]. Hence, if $b_{v\,\rm pen} \gg 10\,\rm G$ then mode penetration at the $-8/2$ resonant surface is effectively impossible.

Shielding breaks down when $-q_{95} < 3.8$ because the $-8/2$ resonant surface is located in the cold resistive plasma at the bottom of the pedestal. Hence, as discussed in Section 1.3, we would expect the application of a $-8/2$ RMP to the plasma when $-q_{95} < 3.8$ to give rise to a density pump-out, rather than ELM suppression [18]. Shielding breaks down if $-q_{95}$ lies in a narrow window of values centered on $-q_{95} = 4.55$ because (as can be seen from Figure 3) the natural phase velocity passes through zero when $-q_{95} = 4.55$, so there is insufficient plasma "rotation" at the resonant surface to generate strong shielding. Note that the $-8/2$ resonant surface lies close to the top of the pedestal when $-q_{95} = 4.55$. As discussed in Section 1.3, we would expect the application of a $-8/2$ RMP to the plasma when $-q_{95}$ lies in the aforementioned narrow window of values to give rise to ELM suppression [18]. On the other hand, we would expect the application of the RMP to the plasma when $-q_{95}$ exceeds 3.8, but does not lie in the narrow window, to merely give rise to strong shielding. It can be seen, from Figure 3, that the width of the window of $-q_{95}$ values in which ELM suppression is possible (which, roughly speaking, corresponds to the range of values for which $b_{v\,\rm pen} < 10\,\rm G$) is about 0.3. This window width is less than the spacing (in q) between the various resonant harmonics of the applied $n = 2$ RMP (which is, of course, 0.5), implying that the $-q_{95}$ windows in which the various resonant harmonics of the RMP can cause ELM suppression in DIII-D discharge #158115 do not overlap.

According to [17], there is a strong correlation between successful RMP-induced ELM suppression in DIII-D plasmas and the $\mathbf{E}\times\mathbf{B}$ frequency, ω_E, passing through zero at a resonant surface located close to the top of the pedestal, but no correlation whatsoever with the linear natural phase velocity, $\varpi_{\perp\, e}$, passing through zero at some such surface. It turns out that, for the case illustrated in Figure 3, $-n\,\omega_E$ and the nonlinear natural phase velocity, ϖ_0, take very similar values when $-q_{95} \simeq 4.55$. Hence, the observations reported in [17] are more consistent with the nonlinear mode penetration model presented in this paper than mode penetration models that employ linear layer physics (which, inevitably, conclude that mode penetration is correlated with $\varpi_{\perp\, e}$ passing through zero).

7.3. Plasma Resistivity Dependence

Figure 4 illustrates what happens to the calculation shown in Figure 3 if we take the experimental resistivity profile and scale it up by a constant factor. It can be seen that by the time the resistivity profile has been increased by a factor 16 the strong shielding of driven magnetic reconnection in the interior of the pedestal that is apparent in Figure 3 has completely disappeared. This illustrates an important point. Although it might be tempting to reduce the run time of a nonlinear-MHD simulation of RMP-induced ELM suppression by increasing the plasma resistivity above its experimental value [45], doing so risks completely changing the nature of the plasma response to the RMP. If there is strong shielding in the interior of the pedestal, as we predict for DIII-D discharge #158115, then application of a multi-harmonic RMP with many resonant surfaces in the pedestal is only likely to drive a magnetic island chain of significant width in the cold plasma at the bottom of the pedestal (where there is no shielding) and, possibly, in the hot plasma at the top of the pedestal (where the natural phase velocity is particularly small). Given that the two island chains are relatively far apart, the magnetic field in the pedestal is unlikely to be rendered stochastic by the applied RMP. On the other hand, if there is no strong shielding in the interior of the pedestal, as we predict if we increase the resistivity of DIII-D discharge #158115 by an order of magnitude, then application of a multi-harmonic RMP with many resonant surfaces in the pedestal is likely to drive magnetic island chains of significant width at every resonant surface. In this case, it is almost inevitable that the magnetic field in the pedestal will be rendered stochastic by the applied RMP. We note, finally, that driving a single large magnetic island chain at the bottom of the pedestal causes a much larger reduction in the pedestal density than in the pedestal temperature (because the density gradient at the bottom of the pedestal is larger than the temperature gradient), which offers a plausible explanation of the density pump-out phenomenon [18]. On the other hand, rendering the pedestal stochastic would inevitably cause a significant reduction in the pedestal temperature, as well as the pedestal density, which cannot explain the density pump-out phenomenon.

7.4. Plasma Density Dependence

RMP-induced ELM suppression is generally observed to be much more difficult when the electron number density is comparatively high [15, 16]. In order to gain a better understanding of this phenomenon, we shall crudely simulate the effect of a density increase or decrease in DIII-D discharge #158115 by taking the profiles shown in Figure 2 and multiplying the density by a constant factor: i.e.,

$$n_e(r) \rightarrow \Delta n_e \, n_e(r). \tag{198}$$

Figure 5 illustrates the effect of such a density increase or decrease on the natural phase velocity, the mode penetration and unlocking thresholds, and the shielding factors just before mode penetration and unlocking, at the $-8/2$ resonant surface. It can be seen that increasing/decreasing the plasma density does not strongly affect the natural phase velocity, but leads to a large increase/decrease in the mode penetration threshold and the associated shielding factor (except when the resonant surface lies in the cold plasma at the bottom of the pedestal), and, most importantly, produces a significant shrinkage/expansion of the width of the q_{95}-window in which RMP suppression is possible. Hence, the analytic model presented in this paper is consistent

with experimental observations that RMP-induced ELM suppression becomes more difficult at higher plasma densities. In fact, a careful examination of the model reveals that increasing the plasma density increases both the plasma inertia and the ion collisionality. The increase in the plasma inertia leads to a direct increase in the mode penetration threshold and the associated shielding factor, whereas the increase in the ion collisionality leads to an indirect increase by increasing the ion neoclassical poloidal flow-damping rate.

7.5. Effect of High-Z Impurities

Figure 6 shows how the predictions of our analytic model of RMP-induced ELM suppression for DIII-D discharge #158115 are affected if the carbon impurities are replaced by tungsten impurities (keeping $Z_{\rm eff}$ equal to 2.5, which implies that the tungsten number density is much less than the corresponding carbon number density). It can be seen that the replacement of carbon by tungsten as the main impurity species causes the natural phase velocity at the $-8/2$ resonant surface to shift significantly in the ion diamagnetic (i.e., negative) direction. This shift presumably occurs because the tungsten ions are in the Pfirsch-Schlüter collisionality regime throughout the pedestal, whereas the carbon ions are in the banana regime at the top of the pedestal, and the plateau regime at the bottom. The aforementioned shift causes the opening of an additional very narrow q_{95}-window in which RMP-induced ELM suppression is possible. The $-8/2$ resonant surface is midway up the pedestal when q_{95} lies in this window. The calculation described in this section illustrates the important role that plasma impurities can play in RMP-induced ELM suppression.

8. Application to ITER H-Mode Discharges

8.1. Model ITER H-Mode Discharge

Figure 7 shows the electron number density, electron temperature, safety-factor, and $\mathbf{E}\times\mathbf{B}$ frequency profiles of a model ITER H-mode discharge. The profiles specified in the figure are based on EPED [46, 47] and TGLF [48] predictions [49]. The reference $\mathbf{E}\times\mathbf{B}$ rotation profile (black curve) is characterized by about 10 krad/s rotation close to the top of the pedestal, and about 20 krad/s core rotation. This rotation profile is generated by a combination of an intrinsic torque and the torque associated with 17 MW neutral beam injection power. The intrinsic torque and the momentum confinement time are estimated from dimensionless parameter scans performed on the DIII-D tokamak [50]. The remaining parameters that characterize the discharge are $B_0 = -5.15$ T, $R_0 = 6.38\,{\rm m}$, $a = 1.98\,{\rm m}$, $Z_{\rm eff} = 1.6$, $M_i = 2$, $M_I = 9.1004$ (which corresponds to a deuterium plasma with beryllium impurity ions), and $\chi_\perp = 1\,{\rm m}^2/{\rm s}$. (Note that we are assuming that the ITER equilibrium magnetic field has the same helicity as the DIII-D field, for the sake of easy comparison.) The majority ion, impurity ion, and electron temperatures are all assumed to be equal, and toroidal flow-damping is neglected.

8.2. Edge Safety-Factor Scan

As before, we shall crudely simulate a q_{95}-scan in our model ITER discharge by adding a constant offset to the safety-factor profile [see (197)], while keeping the other profiles fixed. The unmodified equilibrium is characterized by $q_{95} = -3.08$.

Figure 8 specifies how the natural phase velocity, ϖ_0 [see (121)], at the $m = -9/n = 3$ resonant surface depends on q_{95}. For comparison, the figure shows the natural phase velocity predicted by linear theory, $\varpi_{\perp\, e} \equiv -n\,(\omega_E + \omega_{*\, e})_{r=r_s}$. As expected, the nonlinear natural phase velocity is offset from the linear natural phase velocity in the ion diamagnetic direction. In addition, Figure 8 specifies how the mode penetration and unlocking thresholds at the $m = -9/n = 3$ resonant surface, as well as the corresponding shielding factors just before mode penetration and unlocking, depend on q_{95}.

The data shown in Figure 8 is qualitatively similar to that shown in Figure 3. Shielding at the $-9/3$ resonant surface breaks down for $-q_{95} < 2.6$ because the surface is located in the cold resistive plasma at the bottom of the pedestal. Hence, we would expect the application of a $-9/3$ RMP to the plasma when $-q_{95} < 2.6$ to give rise to a density pump-out, rather than ELM suppression [18]. The data shown in the figure indicates strong shielding just prior to mode penetration (i.e., $\mathcal{S} \gg 1$), combined with a large penetration threshold (i.e., $b_{v\,\rm pen} \gg 60\,{\rm G}$), for all values of $-q_{95}$ in the range $-q_{95} > 2.6$, except for a narrow window of values centered at $-q_{95} = 2.93$. Shielding breaks down if $-q_{95}$ lies in this narrow window of values because (as can be seen from the figure) the natural phase velocity passes through zero when $-q_{95} = 2.93$, so there is insufficient plasma "rotation" at the resonant surface to generate strong shielding. As before, the $-9/3$ resonant surface lies close to the top of the pedestal when $-q_{95} = 2.93$. We would expect the application of a $-9/3$ RMP to the plasma when $-q_{95}$ lies in the aforementioned narrow window of values to give rise to ELM suppression [18]. On the other hand, we would expect the application of the RMP to the plasma when $-q_{95}$ exceeds 2.6, but does not lie in the narrow window, to merely give rise to strong shielding.

The ITER ELM control system is designed to have twice the (relative to the toroidal magnetic field strength) capability of the present DIII-D system [51, 52]. Hence, we infer that the maximum practical amplitude of the vacuum radial magnetic field at the plasma boundary, b_v, for a particular helical harmonic of an applied $n = 3$ RMP, is typically about 60 G. It follows from Figure 8 that the width of the window of q_{95} values in which $n = 3$ ELM suppression is possible in ITER (which, roughly speaking, corresponds to the range of values for which $b_{v\,\rm pen} < 60\,{\rm G}$) is about 0.1. This is slightly smaller than the window width for effective ELM control in DIII-D with an $n = 2$ RMP that we found in Section 7.

Figure 8 also illustrates what happens if the core $\mathbf{E} \times \mathbf{B}$ rotation in ITER falls below $\omega_E = 20$ krad/s. It can be seen that reducing the core rotation increases the shielding in the pedestal, but reduces that in the core. Consequently, as the core rotation falls, the width of the $-q_{95}$ window in which mode penetration is possible increases. However, if the core rotation falls significantly below 5 krad/s then shielding is lost in the core, which renders the plasma very vulnerable to core-resonant locked modes.

8.3. Effect of High-Z Impurities

Figure 9 shows how the predictions of our analytic model of RMP-induced ELM suppression for a model ITER H-mode discharge are affected if the beryllium impurities are replaced by tungsten impurities (keeping $Z_{\rm eff}$ the same). It can be seen that the replacement of beryllium by tungsten as the main impurity species causes a subtle modification in the natural phase velocity profile which, in turn, causes the

window of q_{95} values in which ELM suppression is possible to shift position slightly. Given that successful RMP-induced ELM control in ITER essentially boils down to locating the aforementioned window, the calculation presented in this section again highlights the important role that impurities play in the theory of ELM suppression.

9. Summary and Conclusions

We have developed an analytic theory of ELM suppression in an H-mode tokamak plasma via the application of a static, externally generated, RMP. (See Sections 2–6.) This theory is based on the plausible hypothesis that mode penetration at the top of the pedestal is a necessary and sufficient criterion for RMP-induced ELM suppression [18]. The theory also makes use of a number of key insights obtained in [24]. The first insight is that the response of the plasma to a particular helical component of the RMP, in the immediate vicinity of the associated resonant surface, is governed by nonlinear magnetic island physics, rather than by linear layer physics. This has two important consequences. First, the shielded state consists of a rotating, pulsating island chain, rather than a stationary island chain. (See Section 5.) Second, the so-called natural phase velocity of the driven island chain (i.e., its preferred phase velocity in the absence of the RMP) is quite different to that predicted by linear theory. According to linear layer theory, a naturally unstable island chain propagates in the electron diamagnetic direction relative to the local guiding center frame. However, according to nonlinear island theory, the island chain propagates in the ion diamagnetic direction relative to the local guiding center frame. (See Section 4.4.) This is significant because both the degree of shielding and the mode penetration threshold at the resonant surface depend crucially on the natural phase velocity. The second insight is that neoclassical effects play a vital role in the physics of mode penetration. This is the case, firstly, because intrinsic neoclassical poloidal rotation is the main controlling factor that determines the natural phase velocity of a nonlinear magnetic island chain (see Section 4.4), and, secondly, because neoclassical poloidal flow-damping plays a very significant role in determining the mode penetration threshold. The final insight is that plasma impurities play an important role in the physics of mode penetration. This is the case because impurities can significantly modify both the intrinsic neoclassical poloidal rotation and the neoclassical poloidal flow-damping rate.

The theory developed in this paper has been used to gain a better understanding of the physics of RMP-induced ELM suppression in DIII-D and ITER H-mode discharges. (See Sections 7 and 8.) It is found that ELM suppression is only possible when q_{95} takes values that lie in certain narrow windows. (See Sections 7.2 and 8.2.) Moreover, the widths of these windows decrease with increasing plasma density. (See Section 7.4.) The location and widths of the windows are also sensitive functions of both the concentration and the masses of the plasma impurities. (See Section 7.5 and 8.3.) The window width for a model ITER H-mode discharge is found to be similar to, but slightly smaller than, the window width in a typical DIII-D H-mode discharge.

There are a number of improvements that could be made to the theory described in this paper. Such improvements include; 1) taking into account the coupling of different resonant surfaces via mode-penetration-induced changes in the plasma rotation, density, and temperature, profiles in the pedestal [18]; 2) taking into account the coupling of different poloidal harmonics of the RMP due to toroidicity, the Shafranov shift, and flux surface shaping [53]; 3) employing a more realistic plasma equilibrium; 4) including island saturation terms [54, 55, 56], the perturbed bootstrap

current [57], and the perturbed ion polarization current [58], in the Rutherford equation; 5) taking into account orbit-squeezing effects due to the strong shear in the radial electric field that is typically present in H-mode tokamak pedestals [59]; 6) taking neoclassical toroidal flow-damping into account; 7) allowing for multiple impurity species; and 8) taking into account the fact that high-Z impurities can easily acquire supersonic neoclassical velocities [60].

Acknowledgements

This research was funded by the U.S. Department of Energy under contract DE-FG02-04ER-54742. The author would like to thank Q.M. Hu, R. Nazikian, C. Paz-Soldan, T.E. Evans, C. Chrystal, and R.D. Hazeltine for helpful discussions.

References

[1] Wagner F *et al.* 1982 *Phys. Rev. Lett.* **49** 1408

[2] Zohm H 1996 *Plasma Phys. Control. Fusion* **38** 105

[3] Den Harden N *et al.* 2016 *Nucl. Fusion* **56**, 026014

[4] Loarte A *et al.* 2003 *J. Nucl. Materials* **313**–**316** 962

[5] Evans T E *et al.* 2004 *Phys. Rev. Lett.* **92** 235003

[6] Liang Y *et al.* 2007 *Phys. Rev. Lett.* **98** 265004

[7] Suttrop W *et al.* 2011 *Phys. Rev. Lett.* **106** 225004

[8] Jeon Y M *et al.* 2012 *Phys. Rev. Lett.* **109** 035004

[9] Sun Y *et al.* 2016 *Phys. Rev. Lett.* **117** 115001

[10] Connor J W *et al.* 1998 *Phys. Plasmas* **5** 2687

[11] Fenstermacher M E *et al.* 2008 *Phys. Plasmas* **15** 056122

[12] Bécoulet M *et al.* 2012 *Nucl. Fusion* **52** 054003

[13] Schmitz O *et al.* 2012 *Nucl. Fusion* **52** 043005

[14] Lanctot M J *et al.* 2013 *Nucl. Fusion* **53** 083019

[15] Paz-Soldan C *et al.* 2015 *Phys. Rev. Lett.* **114** 105001

[16] Nazikian R *et al.* 2015 *Phys. Rev. Lett.* **114** 05002

[17] Paz-Soldan C *et al.* 2019 Nucl. Fusion **59** 056012

[18] Hu Q M *et al.* 2019 *Density dependence of edge-localized-mode suppression and pump-out by resonant magnetic perturbations in the DIII-D tokamak* Submitted to *Phys. Rev. Lett.*

[19] Yu Q *et al.* 2003 *Phys. Plasmas* **10** 797

[20] Yu Q 2010 *Nucl. Fusion* **50** 025014

[21] Yu Q, and Günter S 2011 *Nucl. Fusion* **51** 073030

[22] Fitzpatrick R 1993 *Nucl. Fusion* **33** 1049

[23] Fitzpatrick R 1998 *Phys. Plasmas* **5** 3325

[24] Fitzpatrick R 2019 *Analytic Theory of Edge Localized Mode Suppression by Static Resonant Magnetic Perturbations in the DIII-D Tokamak* Submitted to Nuclear Fusion

[25] Fitzpatrick R 1995 *Phys. Plasmas* **2** 825

[26] Fitzpatrick R 2014 *Phys. Plasmas* **21** 092513

[27] Fitzpatrick R 2018 Phys. Plasmas **25** 082513

[28] Fitzpatrick R 2018 Phys. Plasmas **25** 112505

[29] Nazikian R *et al.* 2018 *Nucl. Fusion* **58** 106010

[30] Ara G *et al.* 1978 *Ann. Phys. (NY)* **112** 443

[31] La Haye R J *et al.* 2003 *Phys. Plasmas* **10** 3644

[32] Buratti P *et al.* 2016 *Nucl. Fusion* **56** 076004

[33] Hirshman S P, and Sigmar D J 1981 *Nucl. Fusion* **21** 1079

[34] Kim Y B, Diamond P H, and Groebner R J 1992 *Phys. Fluids B* **4** 2996

[35] Chung M H *et al.* 2005 *High Energy Density Physics* **1** 3

[36] Furth H P, Killeen J, and Rosenbluth M N 1963 *Phys. Fluids* **6** 459

[37] Rutherford P H 1973 *Phys. Fluids* **16** 1903

[38] Hirshman S P 1978 *Nucl. Fusion* **18** 917

[39] Stix T H 1973 *Phys. Fluids* **16** 1260

[40] Shaing K 2003 *Phys. Plasmas* **10** 1443

[41] Cole A J, Hegna C C, and Callen J D 2008 *Phys. Plasmas* **15** 056102

[42] Chapman B E *et al.* 2004 *Phys. Plasmas* **11** 2156

[43] Abramowitz M, and Stegun I A (eds.) 1965 *Handbook of Mathematical Functions with Formulas, Graphs, and Mathematical Tables* (Dover, New York NY) Chapter 9.

[44] Gradshteyn I S, and Ryzhik I M 1980 *Table of Integrals, Series, and Products, Corrected and Enlarged Edition* (Academic Press, New York NY) Equation 6.521.1.

[45] Orain F *et al.* 2019 *Phys. Plasmas* **26** 042503

[46] Snyder P B *et al.* 2009 *Phys. Plasmas* **16** 056118

[47] Snyder P B *et al.* 2011 *Nucl. Fusion* **51** 103016

[48] Staebler G, Kinsey J, and Waltz R E 2007 *Phys. Plasmas* **14** 055909

[49] Meneghini O *et al.* 2016 *Phys. Plasmas* **23** 042507

[50] Chrystal C *et al.* 2017 *Phys. Plasmas* **24** 056113

[51] Evans T E 2019 *private communication*

[52] Evans T E *et al.* 2013 *Nucl. Fusion* **53** 093029

[53] Fitzpatrick R 2017 *Phys. Plasmas* **24** 072506

[54] Thyagaraja A 1981 *Phys. Fluids* **24** 1716

[55] Escande D F, and Ottaviani M 2004 *Phys. Lett. A* **323** 278

[56] Hastie R J, Militello F, and Porcelli F 2005 *Phys. Rev. Lett.* **95** 065001

[57] Fitzpatrick R 1995 *Phys. Plasmas* **2** 825

[58] Fitzpatrick R 2012 *Plasma Phys. Control. Fusion* **54** 094002

[59] Hinton F L, and Kim Y B 1995 *Phys. Plasmas* **2** 159

[60] Hazeltine R D, and Ware A A 1976 *Phys. Fluids* **19** 1163

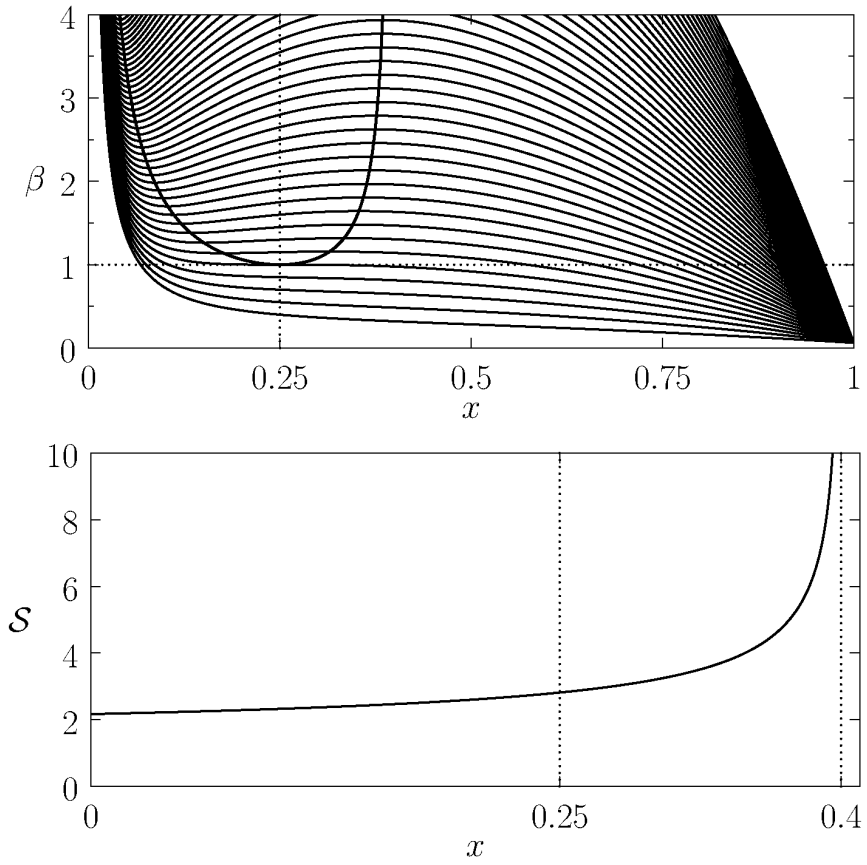

Figure 1. Top Panel: Solutions of the cycle-averaged torque balance equation. The thin curves show constant-γ solutions plotted in x–β space. The curve that passes through the point $x = 1/4$, $\beta = 1$ corresponds to $\gamma = 1$. Curves that pass below (in β) this point correspond to $\gamma < 1$, and vice versa. The solutions lying within the thick curve are dynamically unstable. Bottom Panel: The cycle-averaged shielding factor, $\mathcal{S} = 1/(\langle \hat{W}^{\,4} \rangle_{\varphi})^{\,1/2}$, as a function of normalized plasma rotation at the resonant surface, x, for solutions of the cycle-averaged torque balance equation that lie at the boundary between dynamically stable and dynamically unstable solutions. Low-rotation solutions correspond to $0 \leq x \leq 1/4$, whereas high-rotation solutions correspond to $1/4 < x < 2/5$.

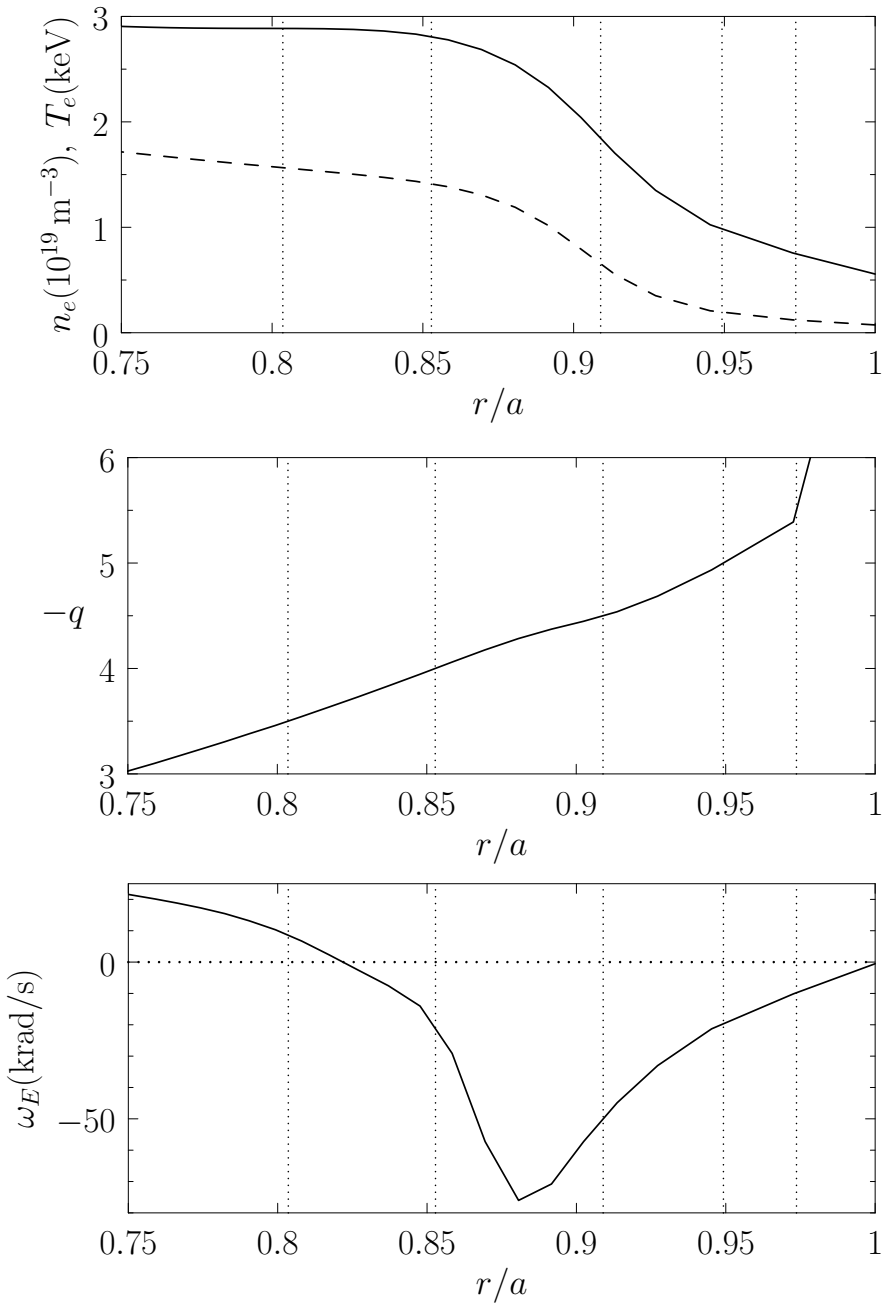

Figure 2. Top Panel: Electron number density (solid curve) and electron temperature (dashed curve) profiles in the pedestal region of DIII-D discharge #158115 at time 3399 ms. Middle Panel: Safety-factor profile in the pedestal region of DIII-D discharge #158115 at time 3399 ms. Bottom Panel: $\mathbf{E} \times \mathbf{B}$ frequency profile in the pedestal region of DIII-D discharge #158115 at time 3399 ms. Here, r is the flux-surface averaged minor radius. The vertical dotted lines show the positions of the -7/2, -8/2, -9/2, -10/2, and -11/2 resonant surfaces, in order from left to right. Data reproduced from Figure 2 of [18].

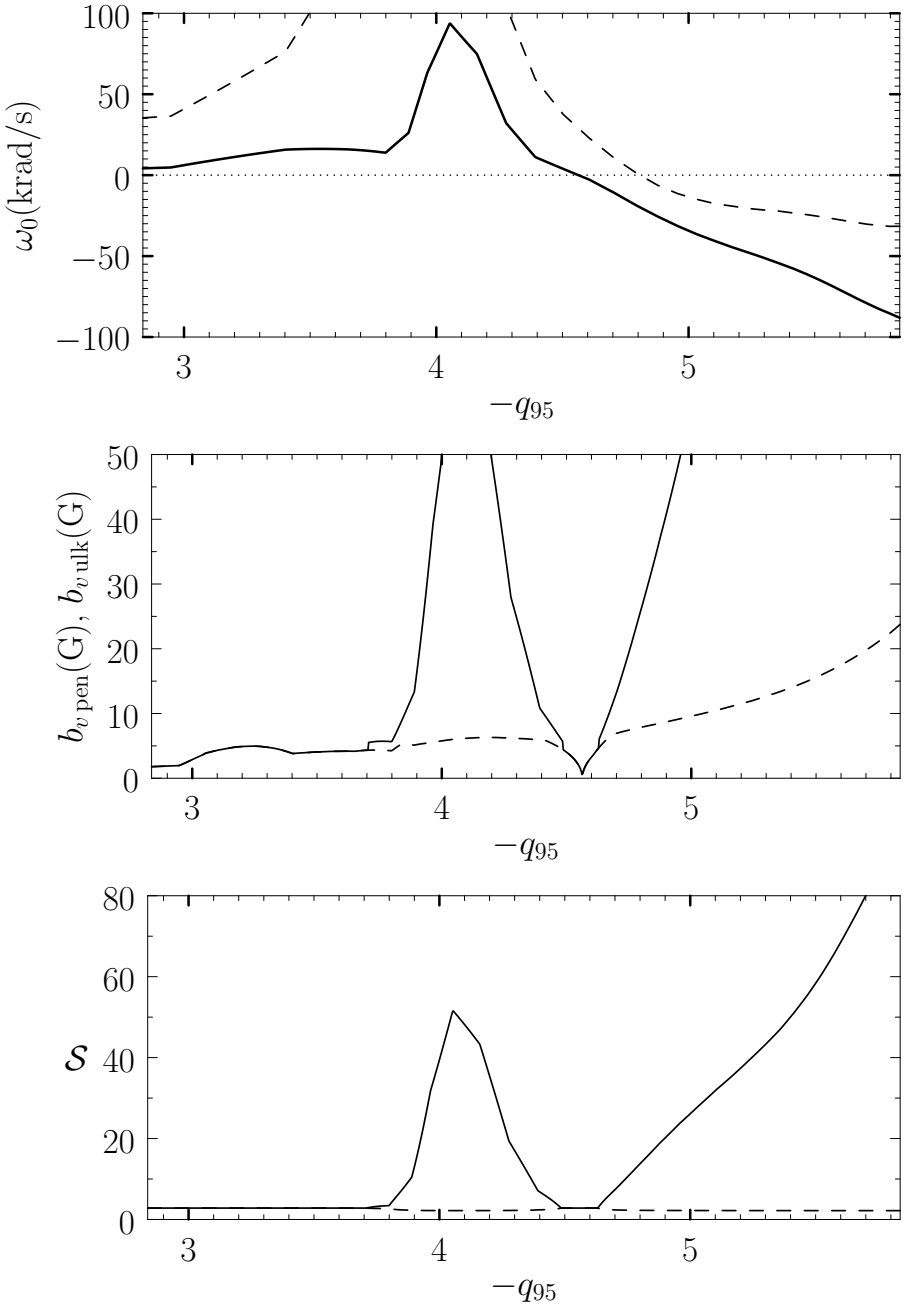

Figure 3. Top Panel: Nonlinear (solid curve) and linear (dashed curve) natural phase velocities at the $-8/2$ resonant surface in DIII-D discharge #158115 as functions of q_{95}. Middle Panel: Mode penetration (solid curve) and unlocking (dashed curve) thresholds at the $-8/2$ resonant surface in DIII-D discharge #158115 as functions of q_{95}. Bottom Panel: Shielding factors just before mode penetration (solid curve) and mode unlocking (dashed curve) at the $-8/2$ resonant surface in DIII-D discharge #158115 as functions of q_{95}.

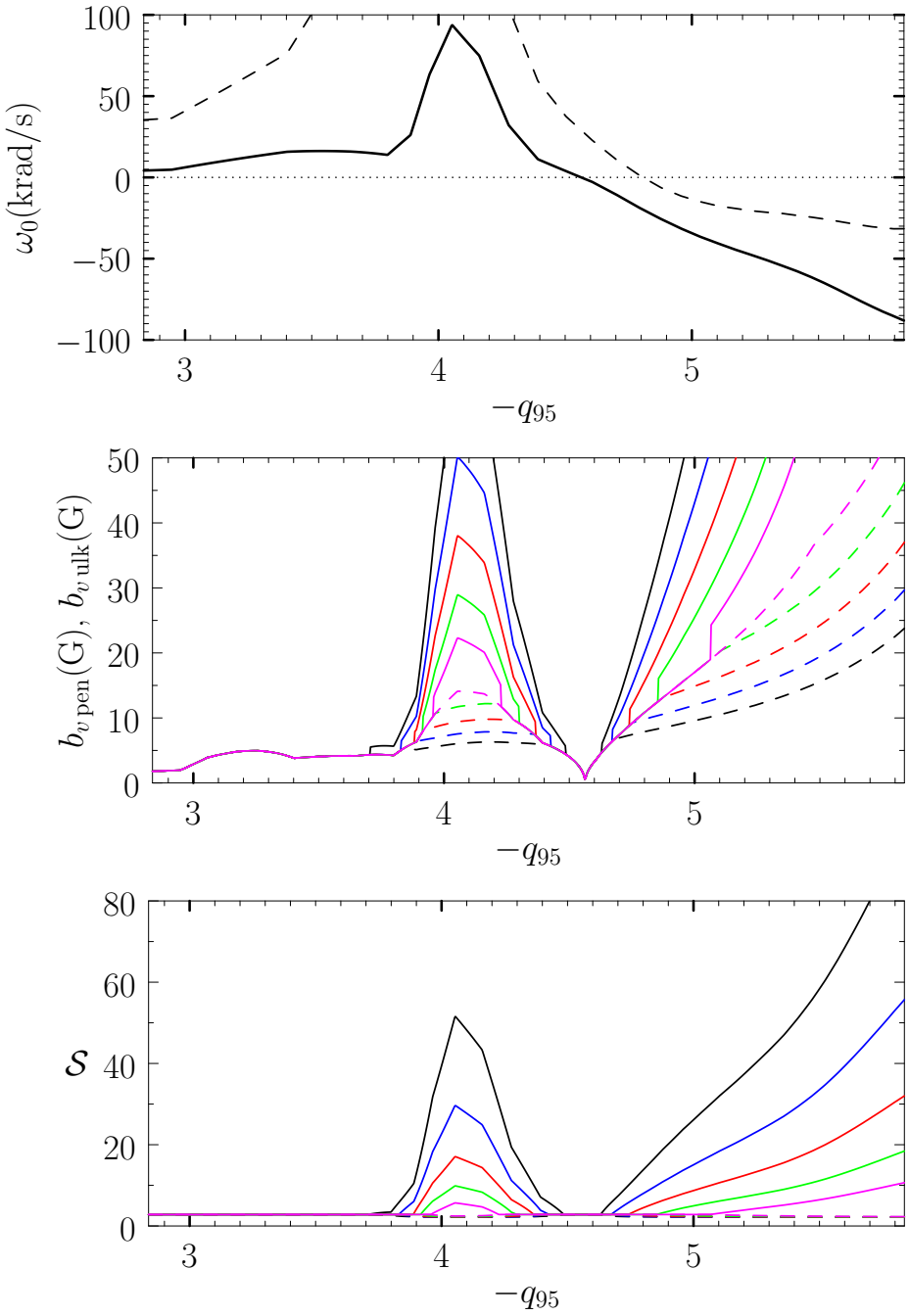

Figure 4. Natural phase velocity, penetration and unlocking thresholds, and shielding factors (see Figure 3 caption) at the $-8/2$ resonant surface in DIII-D discharge #158115 as functions of q_{95}. The black, blue, red, green, and magenta curves correspond to calculations made with the experimental resistivity profile scaled by a factor 1, 2, 4, 8, and 16, respectively.

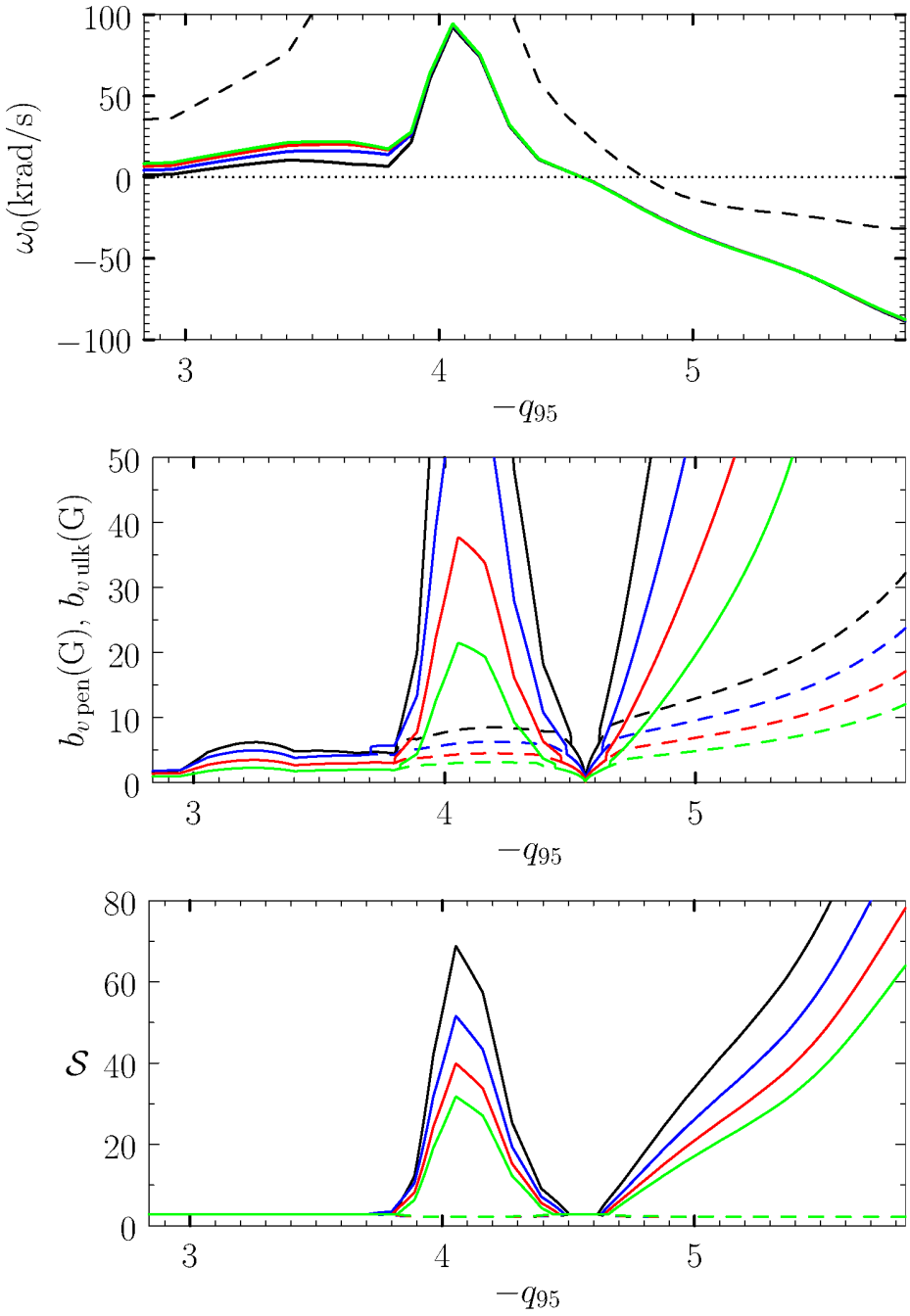

Figure 5. Natural phase velocity, penetration and unlocking thresholds, and shielding factors (see Figure 3 caption) at the −8/2 resonant surface in DIII-D discharge #158115 as functions of q_{95}. The black, blue, red, and green curves are calculated with $n_e(r)$ scaled by a factor 2.0, 1.0, 0.5, and 0.25, respectively, with respect to that specified in Figure 2.

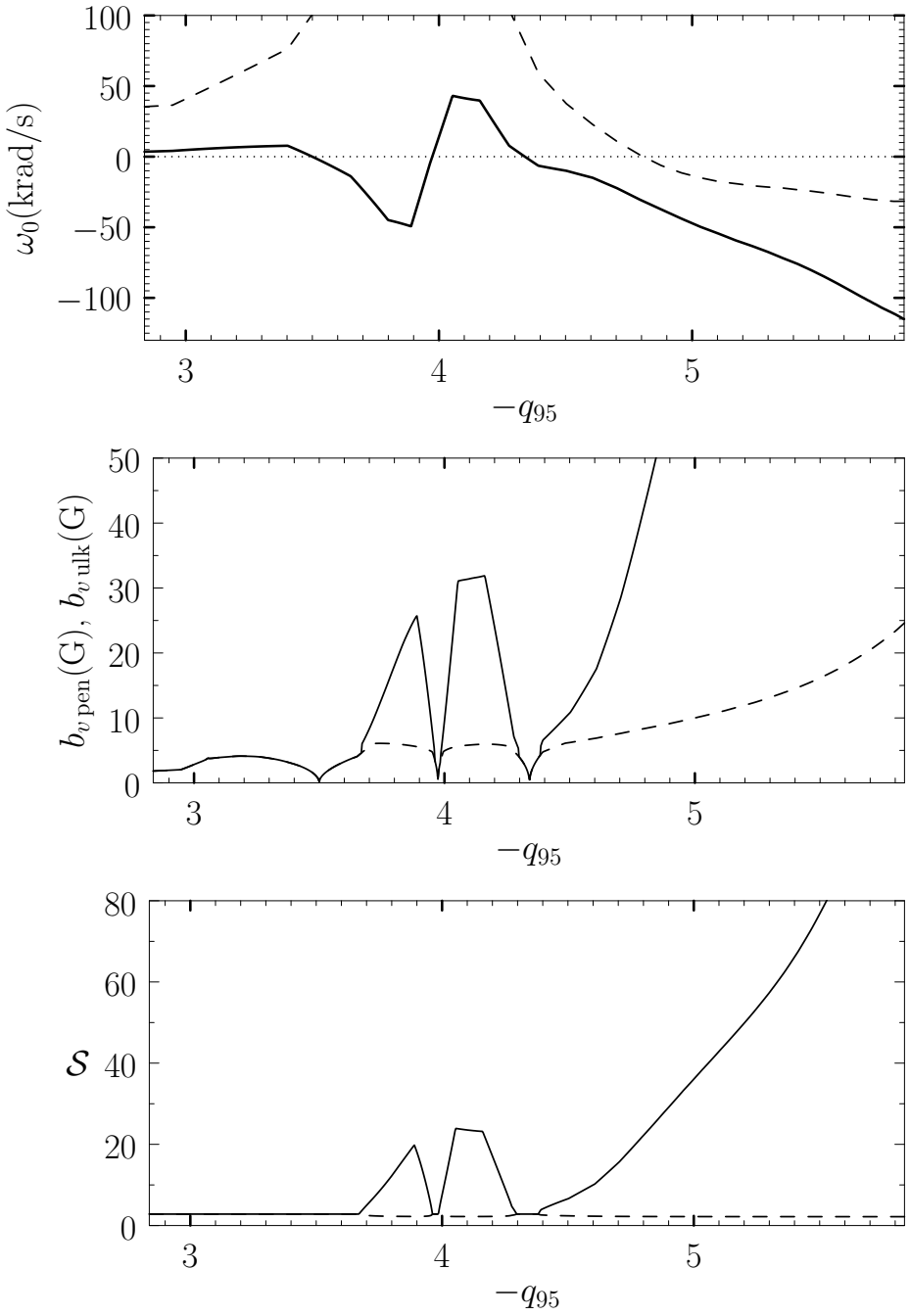

Figure 6. Natural phase velocity, penetration and unlocking thresholds, and shielding factors (see Figure 3 caption) at the $-8/2$ resonant surface in DIII-D discharge #158115 as functions of q_{95}, with tungsten, rather than carbon, as the impurity ion species.

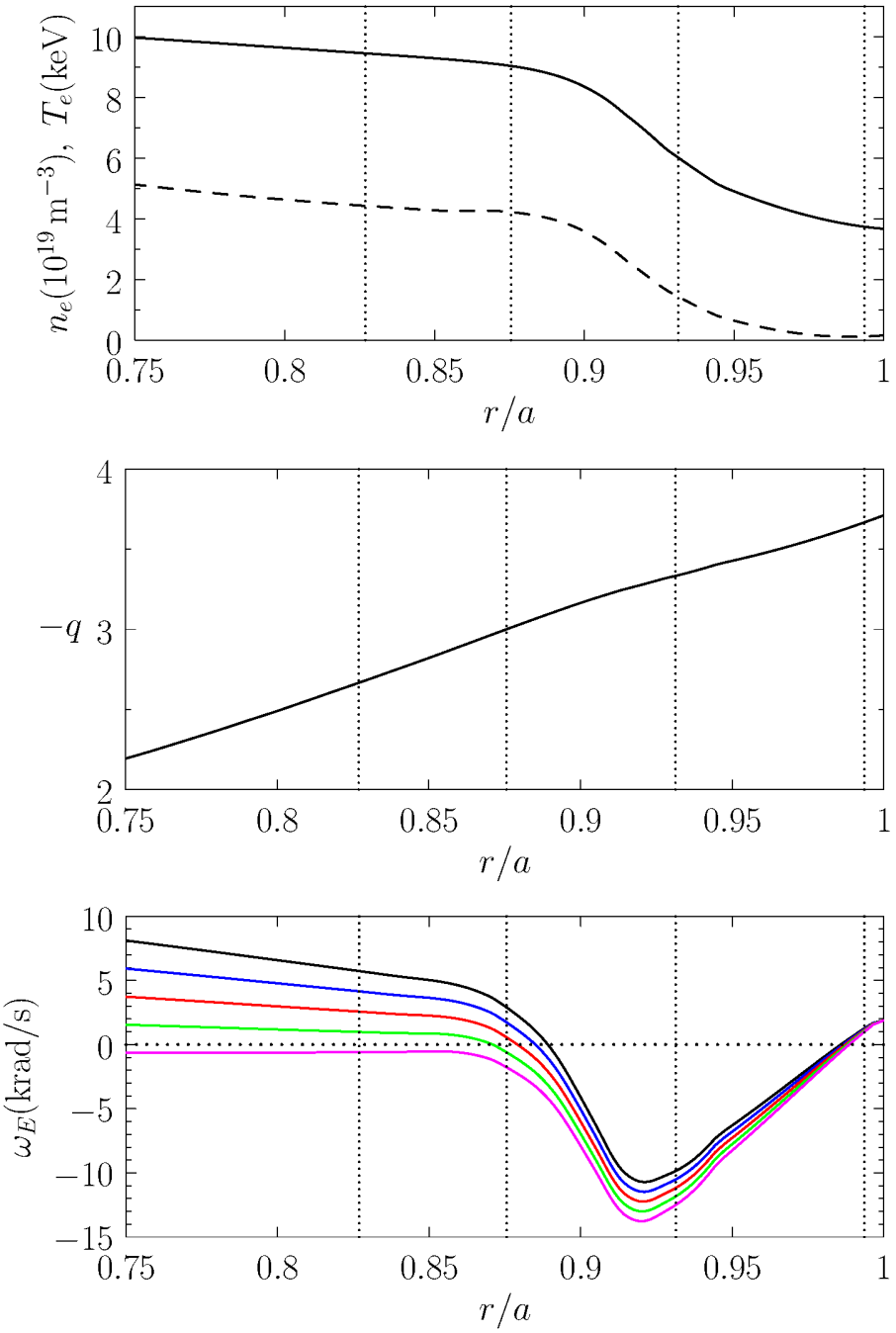

Figure 7. Top Panel: Electron number density (solid curve) and electron temperature (dashed curve) profiles in the pedestal region of a model ITER H-mode discharge. Middle Panel: Safety-factor profile in the pedestal region of a model ITER H-mode discharge. Bottom Panel: $\mathbf{E}\times\mathbf{B}$ frequency profile in the pedestal region of a model ITER H-mode discharge. The black, blue, red, green, and magenta curves correspond to core ω_E values of 20, 15, 10, 5, and 0 krad/s, respectively. Here, r is the flux-surface averaged minor radius. The vertical dotted lines show the positions of the -8/3, -9/3, -10/3, and -11/3 resonant surfaces, in order from left to right.

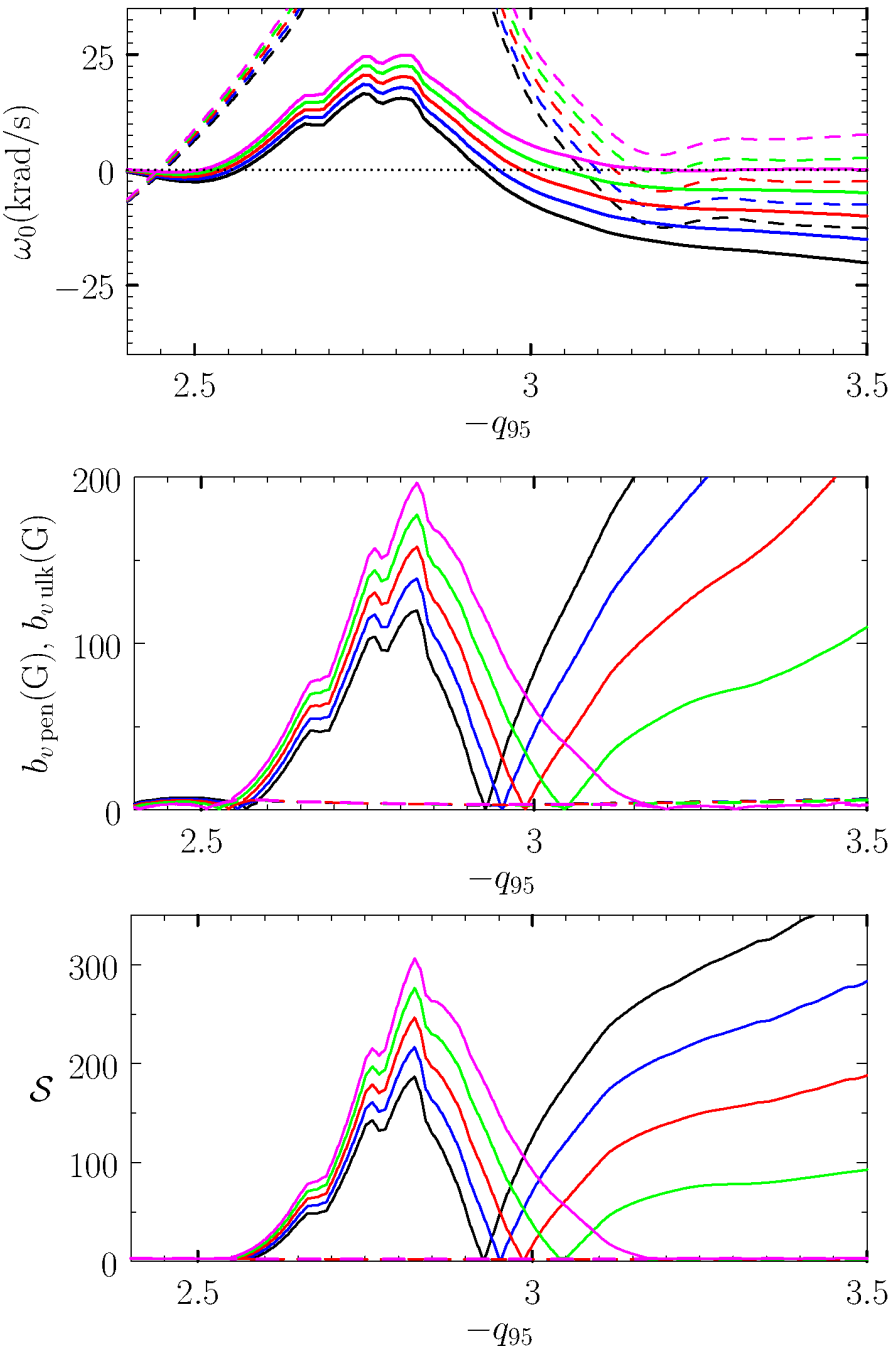

Figure 8. Top Panel: Nonlinear (solid curve) and linear (dashed curve) natural phase velocities at the −9/3 resonant surface in a model ITER H-mode discharge as functions of q_{95}. Middle Panel: Mode penetration (solid curve) and unlocking (dashed curve) thresholds at the −9/3 resonant surface in a model ITER H-mode discharge as functions of q_{95}. Bottom Panel: Shielding factors just before mode penetration (solid curve) and mode unlocking (dashed curve) at the −9/3 resonant surface in a model ITER H-mode discharge as functions of q_{95}. The black, blue, red, green, and magenta curves correspond to core ω_E values of 20, 15, 10, 5, and 0 krad/s, respectively.

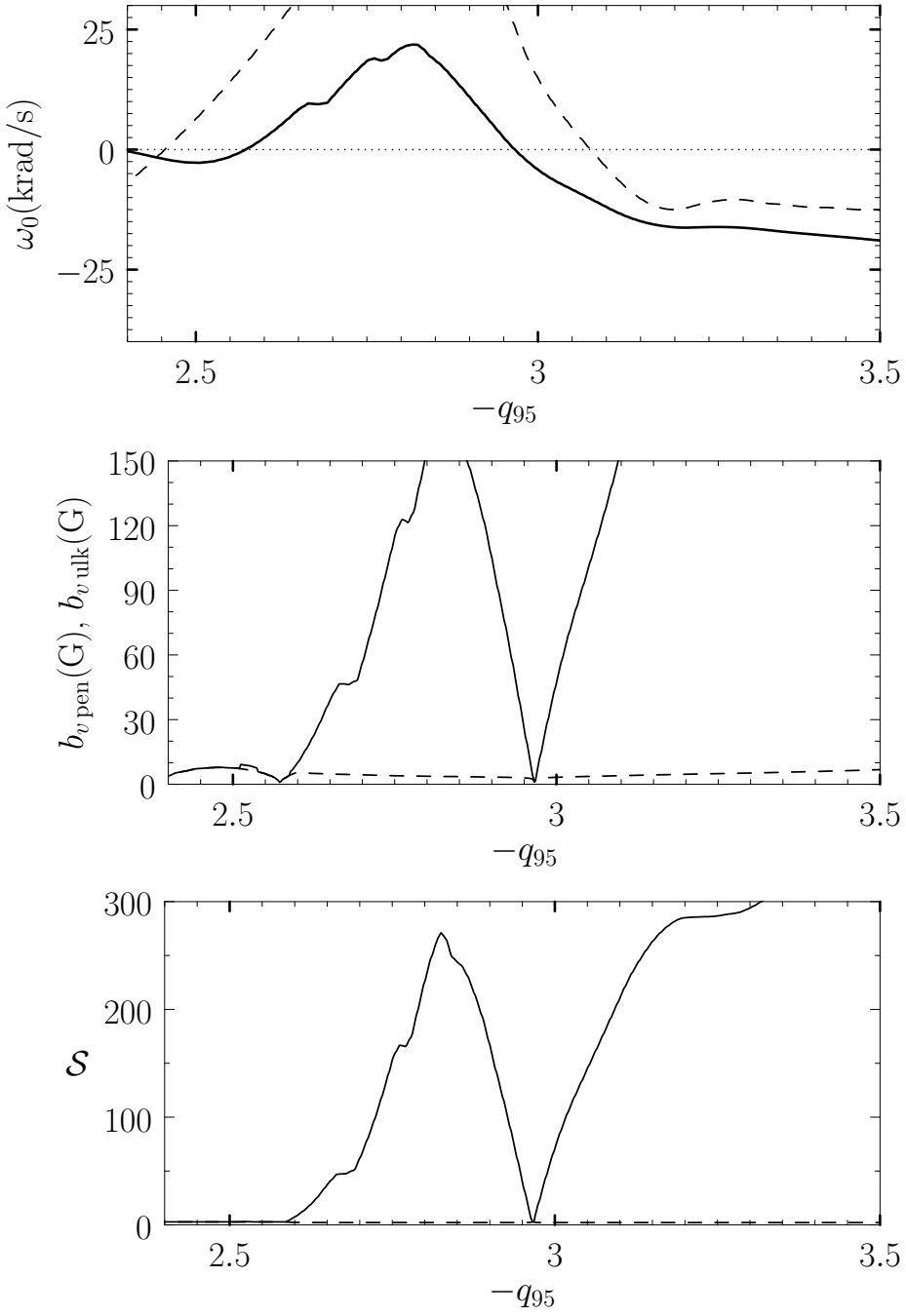

Figure 9. Natural phase velocity, penetration and unlocking thresholds, and shielding factors (see Figure 8 caption) at the $-9/3$ resonant surface in a model ITER H-mode discharge as functions of q_{95}, with tungsten as the impurity ion species (and $\omega_E = 20$ krad/s core rotation).